energies

MDPI

Article

Reducing CO_2 Emissions through the Strategic Optimization of a Bulk Carrier Fleet for Loading and Transporting Polymetallic Nodules from the Clarion-Clipperton Zone

Tomasz Cepowski * and Paweł Kacprzak

Faculty of Navigation, Maritime University of Szczecin, 1-2 Wały Chrobrego St., 70-500 Szczecin, Poland
* Correspondence: t.cepowski@pm.szczecin.pl

Abstract: As global maritime cargo transportation intensifies, managing CO_2 emissions from ships becomes increasingly crucial. This article explores optimizing bulk carrier fleets for transporting polymetallic nodules (PMNs) from the Clarion-Clipperton Zone (CCZ) to reduce CO_2 emissions. Our analysis shows that larger bulk carriers, despite greater drifting forces from environmental conditions, emit less CO_2 over the entire transport mission, including loading and transit. Deploying large ships in global maritime trade could significantly reduce CO_2 emissions. This study also introduces a novel artificial neural network (ANN) model to estimate drifting forces during loading operations and proposes a new method for estimating CO_2 emissions, considering environmental conditions and ship seakeeping properties. These findings highlight the importance of fleet size optimization and effective operational planning in achieving environmental sustainability in maritime transport.

Keywords: maritime carbon management; polymetallic nodules transportation; fleet optimization; artificial neural networks; CO_2 emissions

Citation: Cepowski, T.; Kacprzak, P. Reducing CO_2 Emissions through the Strategic Optimization of a Bulk Carrier Fleet for Loading and Transporting Polymetallic Nodules from the Clarion-Clipperton Zone. *Energies* **2024**, *17*, 3383. https://doi.org/10.3390/en17143383

Academic Editors: Kazimierz Lejda, Artur Jaworski and Maksymilian Mądziel

Received: 13 June 2024
Revised: 5 July 2024
Accepted: 8 July 2024
Published: 10 July 2024

1. Introduction

The 2021 United Nations Conference on Trade and Development report [1] highlights maritime transport as the cornerstone of international trade and the global economic framework. The report indicates that over 80% of global trade volume, particularly in goods, occurs via sea routes. This significant reliance on maritime transportation, in the context of expanding international trade and coupled with numerous pollution control measures targeting other sources, has led to an increasingly substantial contribution of ship emissions to total anthropogenic emissions [2]. Nunes et al. [3] observed that the maritime sector is likely to continue its significant growth alongside global trade. However, the full extent of its impact on the environment, societal aspects, and human health remains unclear. Moreno-Gutiérrez et al. [4] identified the combustion of fuel in ship engines as the primary source of ship-emitted pollutants. Hoang et al. [5] argue that the pursuit of intelligent strategies through the utilization of renewable energy sources, clean fuels, smart grids, and measures for efficient energy use is beneficial for achieving the main IMO objectives, particularly reductions in future CO_2 emissions. Fan et al. [6], in their analysis of ship energy management, justified that managing energy savings and emission reductions is a systemic issue that should be comprehensively considered from multiple perspectives, such as ship design, operational management, and performance assessment. The technical modernization of the ship can also contribute to reducing CO_2 emissions. Barone et al. [7] conducted simulations on a ship equipped with five electric chillers, two auxiliary boilers, two reverse osmosis devices, and two multi-stage flash desalination devices. The simulation results show remarkable energy savings obtained through the proposed optimization approach, corresponding to a fuel consumption reduction of 2.5 kt/y (−1.6 M$/y) and to avoided CO_2 emissions of 8.0 kt/y. The application of solar and wind energy devices affects the reduction in CO_2 emissions. Nyanya et al. [8], in their analysis using a bulk

carrier as an example, demonstrated that considering the optimal sail angle and optimizing the available deck area through the installation of solar and wind systems allowed for the maximum utilization of renewable energy, which contributed to a 36% reduction in carbon dioxide emissions when compared to the same ship without innovative technologies. The conclusions showed that if the ship's speed were reduced to 56% of its original speed, the ship could sail exclusively on renewable energy collected on board. Ytreberg et al. [9] reported that maritime shipping contributes to several environmental challenges, including deteriorations in air quality and human well-being, leading to numerous quantifiable and unquantifiable harms. Their findings demonstrate that transporting goods solely in the Baltic Sea incurs costs due to air quality deterioration, which exceed those associated with climate change impacts.

It is worth noting that oceans and seas serve not only as crucial transport routes for global trade, but also as valuable sources of natural raw materials upon which many industries depend. Recent studies suggest that the deep-sea floor at depths of 4000–6000 m represents a significant source of polymetallic nodules (PMNs), comprising minerals such as manganese (Mn), copper (Cu), cobalt (Co), nickel (Ni), and some rare earth elements [10]. These nodules are considered a promising source of metallic raw materials, with diverse mining systems currently being developed for their extraction [11]. Cunningham [12] concluded that the extraction of nodules from the ocean floor could provide a more stable and decentralized alternative to the current cobalt supplies. The increased cobalt supply from nodule extraction may offset the harmful impacts on the marine environment. Studies by Gollner et al. and Bonifácio et al. [13,14] noted that the extraction process could have adverse environmental effects, impacting biodiversity in the area. Nodule extraction disrupts the composition of seabed sediments, which may lead to long-term negative consequences considering the slow pace of natural habitat recovery. The CC zone features 300 morphotypes, including numerous groups of invertebrates such as corals, crustaceans, and fish [15]. Stratmann [16] argues that conducting extraction operations could lead to an 18% loss of organisms (taxa). B. Li et al. [17] suggests the application of ore separation technology on extraction ships and transporting the separated sediments to land for comprehensive utilization on a separate ship. However, Katona et al. [18] argues that the long-term environmental impact of nodule extraction on marine ecosystems might be lesser when compared to terrestrial mining.

According to recent findings [19], it is anticipated that nodules extracted from the ocean floor will be directly loaded onto high-capacity extraction vessels and transferred to transport ships that will deliver the cargo to destination ports.

During the transfer of nodules from the extraction unit to the transport ship on the ocean surface, the marine environment, i.e., wind and waves, interacts with the transport ship. This can lead to excessive ship swaying, bending, or a loss of stability, as indicated by Kacprzak [20]. In such events, it becomes necessary to suspend the transfer, potentially disrupting the extraction of the nodules from the ocean floor and the operation of the extraction system. Therefore, the transport ship should have the appropriate maritime characteristics to ensure high-efficiency loading and the ability to operate in challenging weather conditions for as long as possible over the mining field, thus minimizing the risk of downtime. An inappropriate selection of transport ships might disrupt the entire extraction system.

According to Kacprzak [21], the transport of PMNs to the destination port can be achieved by both small and large bulk carriers. Research by this author shows that loading onto smaller bulk carriers would lead to shorter loading times and good longitudinal strength, which are significant advantages. However, the disadvantage of these units is their smaller transport capacity, increased ship movement, and poorer stability. On the other hand, large bulk carriers have the advantages of high transport capacity, minimal ship movement, and good stability, with the downside being longer loading times and reduced longitudinal strength.

In addition to the technical limitations with regard to safe loading, a key aspect is the environmental pollution caused by the transporting ship during loading and transport operations. The total CO_2 emissions into the marine environment by the transporting ship depends on the amount of fuel being burned [22]. This amount mainly depends on the power of the dynamic positioning (DP) system which stabilizes the bulk carrier at the loading site, as well as environmental conditions. The required power of the DP system depends on many factors, including the technical parameters of the ship and environmental conditions. Among the technical properties, the size of the ship is most important; according to Jurdziński [23], larger bulk carriers are characterized by a larger windage area, exposed to wind action, and a larger wetted surface, exposed to wave action, which may result in greater drift force. An increase in drift force leads to an increase in the energy needed to maintain the ship position, and thus an increase in pollutant emissions.

In turn, the amount of fuel burned during transport depends on the technical–operational parameters and environmental conditions. The most important technical–operational parameters include ship speed, capacity, the hydro-mechanical properties of the hull, engine efficiency, propulsion system and propeller, type and quality of fuel, draught, trim and hull, and the propeller condition from the fouling process, as mentioned in [24–26]. Environmental conditions affecting fuel consumption include waves, wind, ocean currents, air, and water temperature, as noted in [27]. The reloading and transport of PMNs can be carried out by a fleet of small, medium, and large bulk carriers. Research by Kacprzak [21] has shown that transporting a specified amount of PMNs from the Clarion-Clipperton Zone (CCZ) to the destination requires the consideration of the environmental impact on the technical properties of ships, including stability, motions, and longitudinal strength. Therefore, the bulk carrier fleet should consist of appropriately selected units of various sizes. The key concern is what impact the use of the entire fleet to transport the specified amount of PMNs to different destinations, on routes of varying distances, will have on emissions to the marine environment. Will the use of a fleet of small, medium, or large bulk carriers ensure lower exhaust emissions? How does the distance to the destination port from the CCZ affect this choice? Therefore, the main goal of this study is to answer these questions, i.e., to determine which fleet of bulk carriers (small, medium, large) will be most efficient in terms of environmental CO_2 emissions during the loading and transport of PMNs from the CCZ to various ports around the world.

Studies [28,29] have shown that a large ship can transport a larger amount of cargo at once, burning relatively less fuel during transport to the destination, which translates into less environmental pollution. Therefore, to assess the energy efficiency of the ship, many indicators have been developed, such as

- the energy efficiency operational indicator (EEOI), which is calculated as the ratio of CO_2 emissions to the amount of cargo carried and the distance traveled [30],
- the energy efficiency design index (EEDI), which is expressed as the amount of carbon dioxide CO_2 emitted into the environment based on the estimated fuel consumption in relation to ship capacity and speed [31],
- the annual efficiency ratio (AER), which was created to measure the energy efficiency of a ship based on its annual activity, taking into account the total fuel consumption and distance traveled [32],
- the deadweight tonnage (DWT) efficiency, which determines the efficiency of a ship by the ratio of its cargo capacity (carrying capacity) to fuel consumption,
- the carbon intensity indicator (CII), which measures CO_2 emissions per unit of transport and distance [33].

Chen et al. [34] argue that the ship's EEOI calculated at full load is naturally lower than the equivalent at partial load. The energy efficiency of the fleet shows a slight increase (at least by 1%) due to the implementation of the Ship Energy Efficiency Management Plan. Lee [35] evaluated the possibility of achieving the 40% CO_2 emission reduction target by 2030 through the implementation of the EEDI and the EEXI for three types of ships as follows: bulk carriers, container ships, and tankers. The results show that achieving the 40%

CO_2 emission reduction target by 2030 is possible for ships regulated by the EEDI, while the calculated CO_2 emissions for ships regulated by the EEXI range from 17.4% to 24.6%. This difference arises from the fact that these calculations are based on the maximum speed limit of the EPL's engine output, which exceeds the actual operational speed.

These indicators can be used to assess CO_2 emissions during the transport of nodules. However, they do not consider the energy supplied to the system stabilizing ship movement during reloading operations. During this operation, the transport ship is stationary or moves at a low speed along with the extraction ship, and the DP system stabilizes any ship movement caused by the drift force resulting from wave and wind action. There is no appropriate indicator which assesses the energy efficiency of this process. Therefore, the second goal of the research is to develop a method for estimating CO_2 emissions that considers the impact of environmental conditions on ship loading operations at sea with a cargo of nodules.

2. Materials and Methods

2.1. Data

The subject of the study was a fleet of bulk carriers comprising small, medium, and large ships. Representatives of the three groups of ships were selected for the study. The parameters of these ships are presented in Table 1.

Table 1. Technical parameters of the studied bulk carriers, where L—length between perpendiculars, B—breadth, T—draught, CB—block coefficient, D—displacement, DWT—deadweight, and A_W—lateral plane of the vessel above the plane of draught.

Main Particulars	Ship Size		
	A	**B**	**C**
L [m]	103.9	185	217
B [m]	18.2	24.4	32.26
T [m]	7.057	11.01	14.02
L/B [-]	5.71	7.58	6.73
B/T [-]	2.58	2.22	2.30
L/T [-]	14.72	16.80	15.48
CB [-]	0.80	0.82	0.85
D [t]	11,036	41,900	85,700
DWT [t]	7600	32,000	73,600
A_W [m^2]	746	1711	1977

To compare the efficiency of the different ship types, assumptions regarding the mining system and the locations of the destination ports to which the mined PMNs could be transported were made. It was assumed that the loading of PMNs would take place in the CCZ and would be carried out by the mining ship Hidden Gem. The technical characteristics of this ship are presented in Table 2.

Table 2. Parameters of the mining ship Hidden Gem.

L [m]	228
B [m]	42
T [m]	12
CB [-]	0.82
D [t]	96,504
DWT [t]	61,042

Assumptions regarding the mining system were adopted in accordance with [36] and are presented below:

- the number of planned days for transshipment operations—250 days,
- the assumed annual transport of PMNs—2,000,000 tons,
- the mining capacity of the mining ship—333 tons/h,
- the cargo carrying capacity of the mining ship Hidden Gem—20,000–25,000 t.

It was assumed that the transportation of PMNs from the CCZ would be carried out to the destination ports along the routes described in Figure 1.

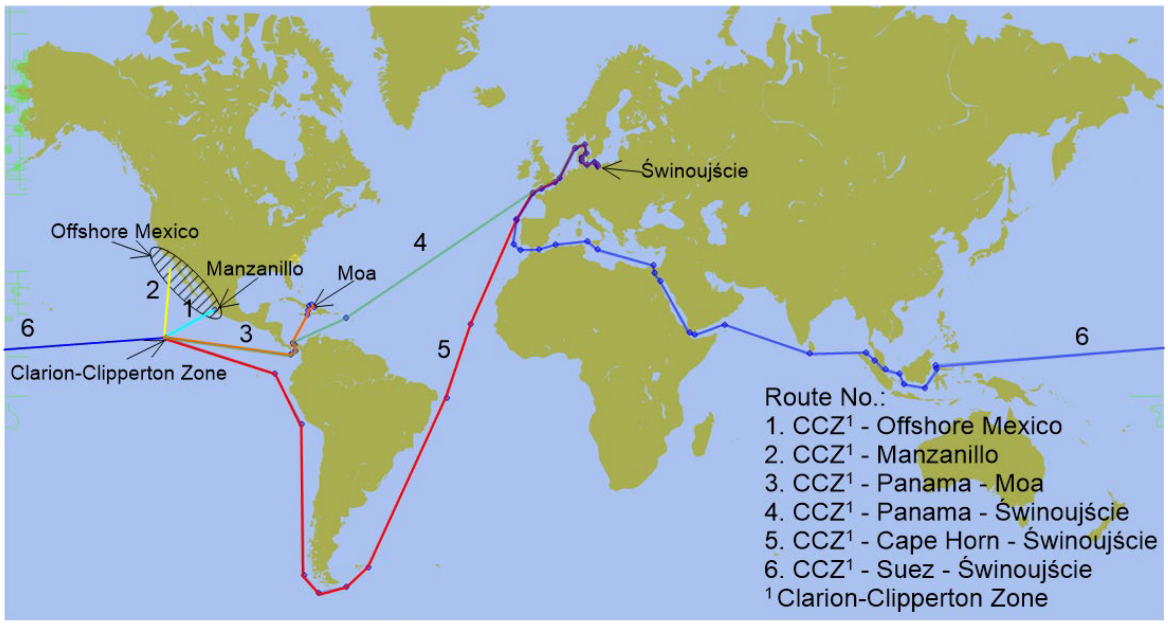

Figure 1. Location of destination ports.

The distribution of wave parameters in the CCZ was developed based on data from [37] and is presented in Table 3. These distributions relate to the occurrence frequency of these parameters throughout the year.

Table 3. Annual frequency of wave parameter occurrence p_{wave} in the CCZ. Data adapted from [37], where Hs—significant wave height and T_z—average zero-up-crossing wave period.

Hs (m)	T_z (s)										
	<4	**4 to 5**	**5 to 6**	**6 to 7**	**7 to 8**	**8 to 9**	**9 to 10**	**10 to 11**	**11 to 12**	**12 to 13**	**>13**
7 to 8	0	0	0	0	0	0.0001	0.0001	0.0001	0.0001	0.0001	0
6 to 7	0	0	0	0	0.0002	0.0005	0.0007	0.0006	0.0004	0.0002	0.0001
5 to 6	0	0	0	0.0003	0.0014	0.0027	0.0031	0.0023	0.0013	0.0006	0.0002
4 to 5	0	0	0.0003	0.0025	0.0081	0.0129	0.012	0.0077	0.0037	0.0014	0.0005
3 to 4	0	0.0001	0.0023	0.015	0.037	0.0455	0.0339	0.0176	0.007	0.0023	0.0006
2 to 3	0	0.0008	0.0143	0.0623	0.1054	0.0928	0.0514	0.0204	0.0064	0.0017	0.0004
1 to 2	0.0001	0.0057	0.0474	0.11	0.1092	0.0605	0.0223	0.0062	0.0014	0.0003	0
0 to 1	0.0005	0.0064	0.0191	0.0185	0.0082	0.0021	0.0004	0.0001	0	0	0

The distribution of wind parameters in the CCZ was adopted in accordance with data from [38] and is presented in Table 4.

To estimate the drift force (F_{wy}), results from ship model tests, the dimensions of which are presented in Table 5, were utilized. These results are based on the studies [39–44] and

include the nondimensional drift force coefficient (C_{wy}), calculated using the following equation:

$$C_{wy} = \frac{F_{wy}}{\rho \cdot g \cdot \varsigma_a^2 \cdot L} \quad (1)$$

where

C_{wy}—nondimensional drift force coefficient,
F_{wy}—mean drift force in a regular wave,
ρ—seawater density,
g—gravity acceleration,
ς_a—amplitude of a regular wave,
L—length of the ship.

All data from these model tests are publicly available, and the references for each dataset are provided in Table 5. Figure 2 shows the values of the drift force coefficient (C_{wy}) in regular waves for these ship models at zero speed as a function of the ratio of the wavelength (λ) to the length of the ship (L). Based on the nondimensional coefficient C_{wy}, calculated using Equation (1) for the ship model scale, it is possible to determine the drift force F_{wy} for a full-scale ship of length L.

Table 4. Distribution of wind speed. Data adapted from [38], where Hs—the significant wave height, v_W—the wind velocity, and p_{wind}—the annual frequency of wind occurrence.

Hs (m)	v_W (m/s)	p_{wind} [-]
1	7.3	0.240
2	10.0	0.270
3	12.1	0.170
4	15.4	0.115
5	19.3	0.091
6	22.1	0.037
7	24.9	0.037
8	27.0	0.020

Table 5. Design characteristics of ship model subjected to model test on mean drift force, where L—length between perpendiculars, B—breadth, T—draught, and CB—block coefficient.

Ship	L/B (-)	B/T (-)	L/T (-)	CB (-)	References
VLCCb	5.52	3.01	16.62	0.81	[43,44]
KVLCC2	5.52	2.79	15.4	0.81	[40,41]
Bulk carrier	5.7	2.7	15.39	0.83	[39]
Scb84	5.52	2.79	15.4	0.84	[42]

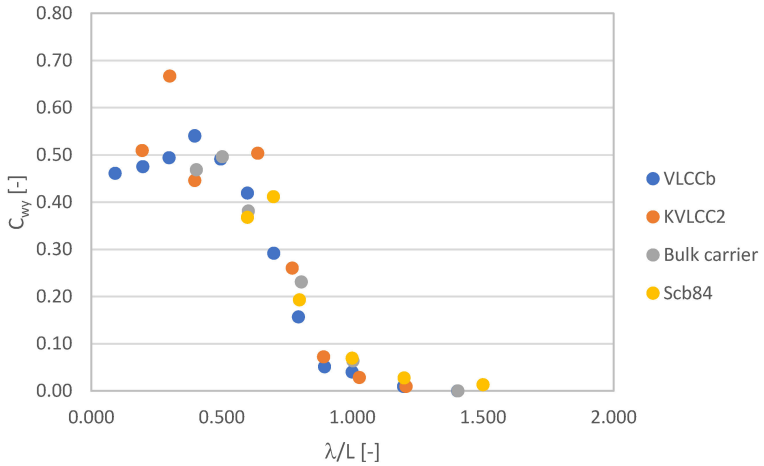

Figure 2. Drift force coefficients of four ships in regular beam waves at zero speed.

2.2. General Research Framework

To achieve the research objective, the estimation of CO_2 emissions during the loading and transportation of PMNs to various long-range destinations was identified as a key step. This estimation was conducted for each type of bulk carrier fleet, designated as A, B, and C, as described in Table 1, depending on the location of the destination port to which the PMNs were to be delivered.

Accordingly, the total CO_2 emission is made up of emissions during loading and transportation as follows:

$$CO_2 = CO_{2load} + CO_{2transp}, \quad (2)$$

where

CO_2—total CO_2 emissions by bulk carrier fleets A/B/C,

CO_{2load}—CO_2 emissions by bulk carrier fleets A/B/C during loading,

$CO_{2transp}$—CO_2 emissions during transportation to the destination port using the bulk carrier fleets A/B/C.

In this study, it was assumed that loading from the mining ship could be executed concurrently with the extraction of PMNs and continuously without breaks for nodule reloading.

2.2.1. Estimation of CO_2 Emissions during Polymetallic Nodules Loading in the Clarion-Clipperton Zone

Figure 3 illustrates a general block diagram for the estimation of CO_2 emissions while nodule loading in the CCZ. The calculation of CO_2 emissions during the loading process is based on the fuel consumption of the transporting bulk carrier while it loads PMNs from the extraction ship as follows:

$$CO_2 = EF \cdot FC\ [t] \quad (3)$$

where

FC—fuel consumption,

EF—emission factor, whose value for a marine engine can be assumed as approximately 3.206 kg CO_2/kg for marine diesel oil (MDO) or approximately 3.114 kg CO_2/kg for heavy fuel oil (HFO).

The fuel consumption during this operation stems from the necessity to generate thrust via the propeller of the DP system to balance out environmental forces, thereby maintaining the ship position during loading under the specified environmental conditions. This fuel consumption (FC) was calculated based on the general relation as follows:

$$FC = P \cdot t \cdot FOC \quad (4)$$

where

P—power supplied to the DP system [kW],

t—time under specified environmental conditions [s],

FOC—fuel consumption rate.

Equation (4) finds extensive application in the analysis and estimation of fuel consumption, both under operational conditions and in the design of ship propulsion systems. A crucial component of this Equation is the fuel consumption rate (FOC), whose values can be derived from the nominal fuel consumption of the marine engine or from real-time fuel flow measurements under operational conditions. The typical FOC values range from 0.170 to 0.185 kg/kWh for marine diesel oil (MDO) and marine gas oil (MGO), and from 0.195 to 0.230 kg/kWh for heavy fuel oil (HFO), depending on the engine type and the operational conditions.

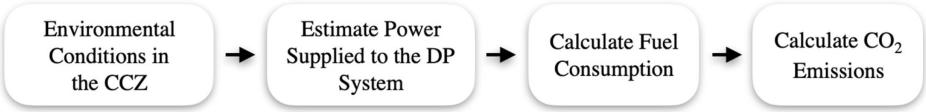

Figure 3. General research scheme for the calculation of CO_2 emissions during loading.

The required power supplied to the propellers of the DP system can be calculated based on the following formula [45]:

$$P = Tp/Cp \quad (5)$$

where

P—propeller power [kW],

Tp—thrust force of the DP system propeller required to overcome environmental forces [kN],

Cp—power-to-thrust efficiency ratio for the given propeller; for tunnel thrusters, Cp = 0.12–0.16.

The calculation of propeller thrust force generally considers the wind drift force, wave drift force, and current drift force. Given that the CCZ, located in the Pacific between Hawaii and Mexico, is known for its slow-moving ocean currents with a maximum speed of approximately 0.3 m/s [37] and given the negligible speed of the ship, the influence of ocean currents on the ship was omitted in this study. Therefore, the thrust force (Tp) was calculated as follows:

$$Tp = F_w + F_{wy} \quad (6)$$

where

F_w—force from wind pressure,

F_{wy}—force from wave drift.

The magnitude of forces from wind and waves depends on their direction relative to the ship. Given the lack of detailed information about wave and wind directions in the CCZ, this study assumes that waves and wind impact the ship unfavorably, i.e., perpendicular to the beam. The force from wind pressure is calculated as follows:

$$F_w = \frac{1}{2} \cdot v_W^2 \cdot \rho \cdot A_w \quad (7)$$

where

v_W—wind speed according to Table 4,

ρ—air density,

A_w—the lateral plane of the vessel above the plane of draught according to Table 1.

The wave drift force was calculated based on the following relation:

$$F_{wy} = L \cdot \rho \cdot g \cdot \int S_{\zeta\zeta}(\omega) \cdot C_{wy}(\omega) d\omega \quad (8)$$

where

F_{wy}—mean wave drift force from irregular waves [kN],

L—ship length [m],

ρ—seawater density,

g—acceleration due to gravity,

$S_{\zeta\zeta}$—wave spectral function,

C_{wy}—mean nondimensional sway force in regular wave.

The wave spectrum function was implemented according to the ITTC guidelines [46] as follows:

$$S_{\zeta\zeta}(\omega) = A\omega^{-5} \exp\left(-B\omega^{-4}\right) \quad (9)$$

where

A, B—coefficients calculated as follows:

$$A = \frac{173\ H_s^2}{T_z^4} \tag{10}$$

$$B = \frac{691}{T_z^4} \tag{11}$$

H_S—significant wave height,
T_z—zero-up-crossing wave period,
ω—circular frequency.

To calculate the drift force, numerical methods, such as the far-field and near-field pressure methods, as well as experimental studies, are used. Far-field methods, initiated by Maruo [47], further developed by Newman, Salvesen, Gerritsma, and Beukelman [48–50] and most recently by Kashiwagi [51], are based on considerations of the energy of diffracted (reflected and transmitted) and radiated waves, momentum flux at infinity, and work conducted by the body in the near field, leading to a constant force acting through the total rate of momentum change. Alternatively, near-field methods, initiated by Boese [52], calculate second-order constant forces/moments through the direct integration of hydrodynamic, steady second-order pressure acting on the wetted surface of the body. More accurate numerical implementations were later introduced by Faltinsen et al. [53], and then by Papanikolaou and Nowacki [54], which led to an increase in precision. These methods have evolved and been validated based on experimental studies, mainly in terms of the longitudinal component, referred to as additional wave resistance. However, the validation of these methods for a transverse component is limited, mainly due to the scarcity of experimental research. Recently, Liu S and Papanikolaou [55] approximated the mean sway force with an empirical formula, only utilizing main ship particulars and wave parameters.

2.2.2. Application of Artificial Neural Networks to Estimate Mean Nondimensional Sway Force in Regular Waves

The application of artificial neural networks (ANNs) to estimate the nondimensional drift force coefficient in regular waves (C_{wy}) for bulk carriers A, B, and C was assessed using the results of model studies described in Table 5, which are presented in Figure 2. An ANN was used for the estimation process. An additional objective of this study was to examine the effectiveness of ANN use to predict drift force based on the basic dimensions of the ship.

In the field of maritime engineering, the application of ANNs has been increasingly acknowledged for its critical role in enhancing the predictability of the experimental measurements pertinent to ship theory. The development and implementation of ANNs have enabled scientists and engineers to process and interpret extensive datasets efficiently and accurately, significantly improving the accuracy of predictive models in ship design and operational strategies. The integration of ANNs in naval architecture has notably enhanced the accuracy of prognostic models, facilitating substantial advancements in various aspects of ship construction and functionality.

For example, research by Cepowski [56,57] utilized Multilayer Perceptron (MLP) structured neural networks to estimate the additional wave resistance of ships based on fundamental design parameters. This approach resulted in remarkably accurate estimations when compared to outcomes from model experiments. Similarly, Yangjun and Yonghwan [58] applied an ANN to predict sloshing effects in model tests of floating structures larger than conventional LNG carriers. The development of this ANN was based on a thorough analysis of over 540 terabytes of experimental data, covering a wide range of variables, such as cargo hold dimensions, vessel types, and environmental and operational conditions. Furthermore, Dyer et al. [59] employed an ANN to estimate the remaining service life of offshore oil and gas platforms, incorporating a comprehensive dataset representing both natural and engineered aspects of offshore systems. Their findings highlighted

the capacity of ANNs to provide highly accurate predictions, indicating life extension, maintenance, and risk minimization strategies for offshore platforms.

In this study, the development of an ANN to estimate the C_{wy} coefficient utilized ship data from Table 5 and model study results presented in Figure 2. Following [56,57], a Multilayer Perceptron (MLP)-structured ANN was adopted.

Figure 4 illustrates the procedure for developing the ANN. The first step involved normalizing the dataset to the [0, 1] range to accelerate learning, avoid numerical issues such as overflow or underflow, prevent feature domination, facilitate weight initialization, and enhance the performance of algorithms based on gradients or distances. Following this procedure, a set of alternative ANNs was developed, differing in the number of neurons in the hidden layer and activation functions. In each ANN, to detect overfitting, the hold-out method with an additional validation set was applied, consisting of the following steps:

1. randomly splitting the data into three parts: training set (50%), testing set (25%), and validation set (25%),
2. training the model on the training set,
3. applying early stopping to prevent overfitting by monitoring the error on the testing set,
4. testing the model on the testing set after each epoch and calculating performance metrics,
5. validating the model on the validation set after training is complete,
6. calculating final performance metrics and comparing them with the results from the testing set to assess the model's generalization capability,
7. analyzing the results from the validation set to evaluate the model's ability to generalize to new data.

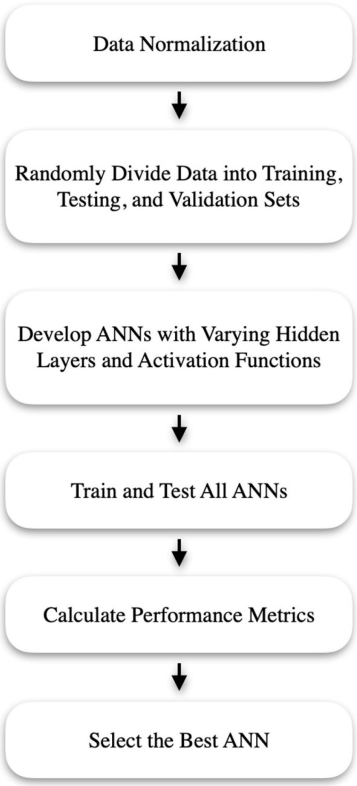

Figure 4. Research scheme for developing an ANN.

In the hold-out procedure, the training and testing process involved early stopping to prevent overfitting by halting the training process if errors increased. The early stopping technique consisted of the following steps:

1. input data: feeding the network with training dataset inputs,
2. prediction: calculating the network's predictions (outputs),
3. error calculation: computing the difference between the predictions and the actual output values using an error function,
4. repetition: repeating steps 1 and 2 for all input–output pairs in the training dataset,
5. weight adjustment: using a learning algorithm to adjust the weights of the neurons to minimize the prediction error,
6. testing: feeding the network with all cases from the testing dataset, obtaining predictions, and comparing them with the actual output values from the dataset to calculate the network error,
7. error comparison: comparing the current network error with the error from the previous cycle. If the error has decreased, the training continues; otherwise, the process is stopped.

The mean absolute error (MAE) was used as the error function in this algorithm, which is defined as follows:

$$\mathrm{MAE} = \frac{\sum_{i=1}^{n} \left| out_{(i)} - out_{p(i)} \right|}{n} \tag{12}$$

where out is the output value, out_p is the predicted output value, and n is the number of instances.

The efficacy of the proposed ANN was assessed using the following established performance metrics: Pearson correlation coefficient (PCC), determination coefficient (R^2), RMSE, and relative RMSE (RRMSE), as delineated in [60,61]. Values of RMSE and RRMSE approaching zero, along with R^2 and PCC values nearing one, indicated a robust alignment between forecast outcomes and empirical data. According to a previous study [62,63], THE estimation accuracy was divided into THE FOLLOWING four categories based on the RRMSE criterion: excellent (below 10%), good (10% to 20%), acceptable (20% to 30%), and unacceptable (above 30%). The performance metrics were calculated as follows:

$$\mathrm{PCC} = \frac{\sum(\mathrm{y}_e - \overline{\mathrm{y}})(\mathrm{y}_\mathrm{e} - \overline{\mathrm{y_e}})}{\sqrt{\sum(\mathrm{y} - \mathrm{y})^2(\mathrm{y}_\mathrm{e} - \overline{\mathrm{y_e}})^2}} \tag{13}$$

- Determination coefficient (R^2):

$$\mathrm{R}^2 = \frac{\sum(\mathrm{y_e} - \overline{\mathrm{y}})^2}{\sum(\mathrm{y} - \overline{\mathrm{y}})^2} \tag{14}$$

- Root mean square error (RMSE):

$$\mathrm{RMSE} = \sqrt{\frac{\sum(\mathrm{y} - \mathrm{y_e})^2}{\mathrm{n}}} \tag{15}$$

- Relative root mean square error (RRMSE):

$$\mathrm{RRMSE} = \frac{\mathrm{RMSE}}{\overline{\mathrm{y_e}}} \times 100 \tag{16}$$

In the final stage, the best ANN was selected based on two criteria as follows:

- highest accuracy of prediction relative to measured data,
- smallest difference between the performance metrics calculated for the training, testing, and validation sets.

2.2.3. Application of Artificial Neural Networks to Estimate Mean Nondimensional Sway Force in Regular Waves

The general Equation (3) presented above for calculating CO_2 emissions is based on Equation (4) for estimating fuel consumption. A key element in calculating fuel consumption is the power supplied to the DP system over time under specified environmental conditions, such as wind and waves. To comprehensively include the impact of wave and wind interaction on fuel consumption, this article expands Equation (4) and proposes a new approach to calculating fuel consumption by considering the impact of wind and waves as follows:

$$FC = FOC \cdot t \cdot \left(\sum_{i=1}^{8} \sum_{j=1}^{11} p_{wave(H_{S(i)}, T_{z(j)})} \cdot P_{wave(H_{S(i)}, T_{z(j)})} + \sum_{i=1}^{8} p_{wind(i)} \cdot P_{wind(i)} \right) \quad (17)$$

where

P_{wave}—power needed to counteract the drift force caused by the wave height Hs and period T_z [kW],

p_{wave}—annual frequency of the wave height (Hs) and period (T_z) in the CCZ according to Table 3 [-],

P_{wind}—power needed to counteract the drift force caused by wind [kW],

p_{wind}—annual frequency of wind occurrence at a given speed according to Table 4 [-].

The above formula takes fuel consumption calculations into account in the case of the wave interaction time at a given height Hs and period T_z and the time of wind interaction at a given speed. These times are calculated based on the wave occurrence frequency and wind parameters presented in Tables 3 and 4.

Equation (17) can be used to calculate fuel consumption and considers the full range of wave and wind parameters, as well as taking a limited range of wave and wind conditions into account, e.g., for waves up to 3 m and corresponding wind speeds.

2.2.4. CO_2 Emissions during Transport

The estimation of CO_2 emissions during maritime transport is based on the energy efficiency design index (EEDI), which, according to the IMO guidelines [31], is defined as the ratio of the CO_2 emitted by a ship per nautical mile to its transport capacity and speed. The calculations considered the threshold values of the EEDI that must be met by each bulk carrier.

Figure 5 illustrates the block diagram for estimating CO_2 emissions during the transport of PMNs to the destination port. The CO_2 emission was calculated using the following formula:

$$CO_{2transport} = EEDI_c \cdot DWT \cdot d_T \quad (18)$$

where

DWT—deadweight tonnage of the bulk carrier from fleet A/B/C [t],

d_T—total distance [NM],

$EEDI_c$—the required energy efficiency design index for bulk carriers A/B/C according to the International Maritime Organization [31] guidelines, calculated as follows:

$$EEDI_c = \frac{1 - X}{100} \cdot 961.79 \cdot DWT^{-0.477} \quad (19)$$

where

$EEDI_c$—the required energy efficiency design index, expressed as the number of grams of CO_2 emissions per nautical mile per ton of cargo,

X—is the reduction factor, whose value for phase 3, according to [31], which starts from 2025, is 30.

The $EEDI_c$ index, calculated using Equation (19), serves as the reference line for determining the required emission reductions within the framework of the energy efficiency design index (EEDI). In calculating the $EEDI_c$, various technical and operational factors

were considered, including deadweight tonnage (DWT), ship type, technical specifications, and operational speed. Weather conditions were also indirectly accounted for through the inclusion of the sea margin and historical data on the actual fuel consumption and CO_2 emissions of ships, which formed the basis for developing the $EEDI_c$. Figure 6 shows the values of $EEDI_c$ for different types of ships depending on the DWT, assuming a reduction factor X, applicable from 2025.

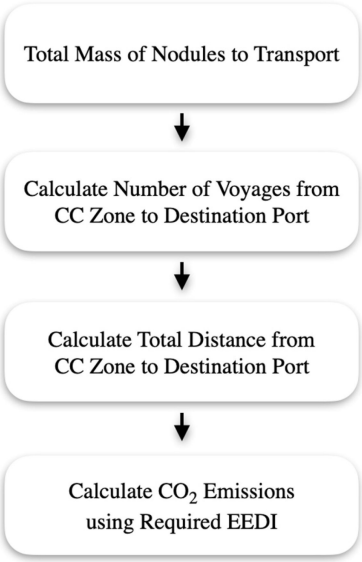

Figure 5. General research scheme for calculating CO_2 emissions during transport.

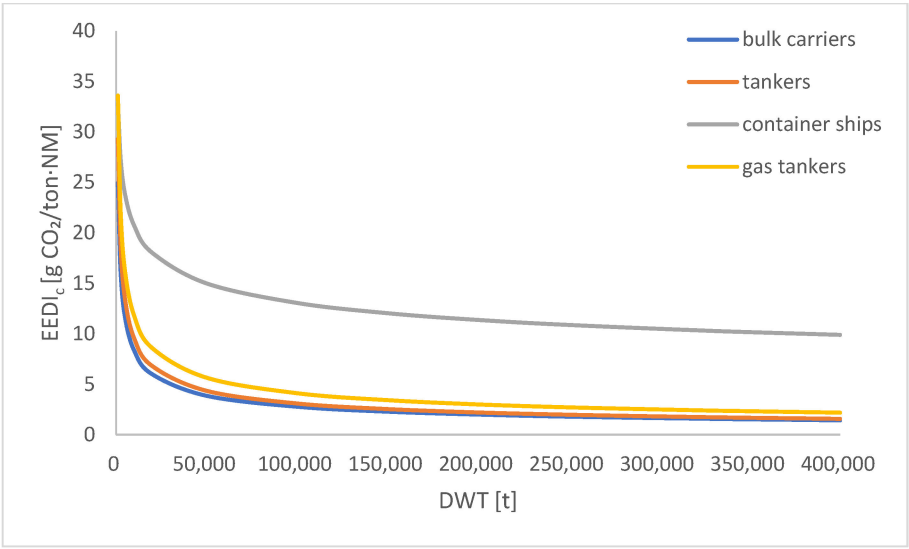

Figure 6. Values of EEDIc for different types of ships as a function of DWT, assuming a reduction factor X, applicable from 2025.

The total distance d_T was calculated based on the formula:

$$d_T = n_{load} \cdot d \quad (20)$$

where

d—distance from the CCZ to the destination port,

n_{load}—number of transfers from the extraction ship to the transporting bulk carrier.

The number of PMN transfers from the extraction ship to the transporting bulk carrier was calculated based on the total assumed mass of nodules to be transferred and the deadweight tonnage of carriers from fleets A, B, and C as follows:

$$n_{load} = M/DWT \quad (21)$$

where

M—total mass of PMNs to be transported, M = 2,000,000 t.

3. Results

3.1. Prediction of a Nondimensional Sway Force Coefficient Using an ANN

A nondimensional sway force coefficient, C_{wy}, was predicted using a Multilayer Perceptron (MLP) neural network structure. The model utilized the following ratios and coefficients that impact the sway force coefficient, C_{wy}:

- L/B (length-to-breadth ratio),
- B/T (breadth-to-draught ratio),
- L/T (length-to-draught ratio, as a combination of L/B and B/T),
- CB (block coefficient),
- λ/L (wavelength-to-ship length ratio).

These features were chosen based on their physical significance and impact on ship hydrodynamics, as supported by the literature [39–44]. This selection ensured that the model utilized the most informative and relevant variables to accurately predict the C_{wy} coefficient.

The training dataset was sourced from publicly available ship model tests, as reported in the literature [39–44]. The design characteristics of the ship models used in these tests are presented in Table 5. The dataset consisted of 32 cases. To evaluate the model's performance and prevent overfitting, early stopping was employed during the network's training. Additionally, the dataset was randomly divided into the following three parts using the hold-out method: training (sixteen cases), testing (eight cases), and validation (eight cases). This approach allowed for the detection and prevention of overfitting by providing separate datasets for model training, validation, and final performance evaluation.

To optimize the learning process, the data were normalized to a range from 0 to 1. This normalization aimed to accelerate learning, avoid numerical issues such as overflow or underflow, prevent feature domination, facilitate weight initialization, and improve the performance of gradient-based algorithms.

During the training of the ANN, additional hyperparameters were used as follows: a learning rate of 0.1, a batch size of 32, and a maximum of 100 epochs. The BFGS optimization algorithm [64–67] was employed, which has proven to be highly effective for training ANNs to predict additional wave resistance [57]. The most accurate neural network identified through this research contained five neurons in the input layer, six neurons in the hidden layer, and one neuron in the output layer. All neurons were activated using a logistic function as follows:

$$\sigma(x) = \frac{1}{1 + e^{x}} \quad (22)$$

where $\sigma(x)$ is the value of the activation function for the input x.

Graphically, the general structure of this ANN is illustrated in Figure 7. Normalization coefficients and weights are provided in Appendix A.

Additionally, during training, early stopping was utilized to prevent overfitting by halting the training process if errors increased for the training and testing data. This process was stopped after 54 epochs, with the stopping condition being a change in error of 1×10^{-5}.

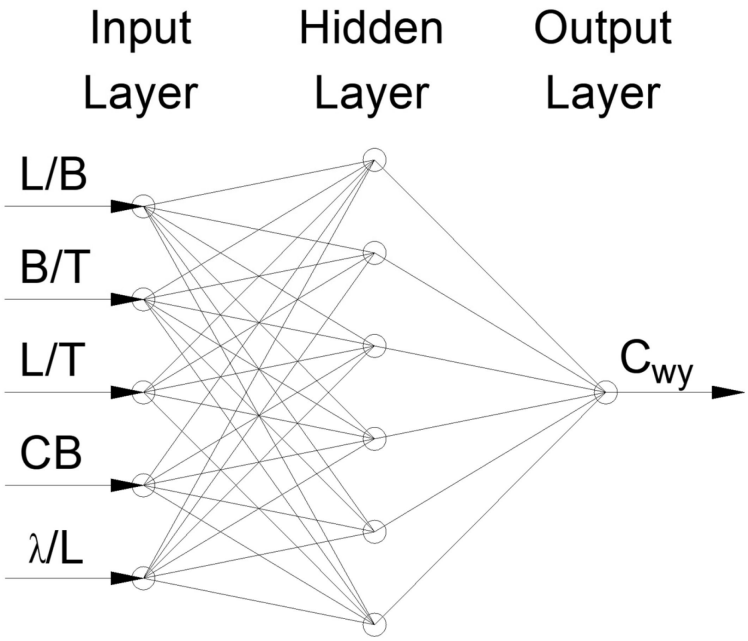

Figure 7. The general structure of an ANN.

To further increase the reliability of the results, four different performance evaluation metrics were applied as follows: Pearson correlation coefficient (PCC), determination coefficient (R^2), root mean square error (RMSE), and relative root mean square error (RRMSE). Table 6 presents these model evaluation metrics for the ANN. This table shows that the PCC values are close to 1, indicating a strong linear correlation between the predicted and actual values for all datasets. High PCC values suggest that the model predictions are well correlated with the actual data. For the training set, the PCC value is 0.98, for the validation set, it is 0.99, and for the test set, it is 0.97. The R^2 values are also high, indicating that the model explains the variability of the data well. High R^2 values mean that the model fits the data well for the training, validation, and test sets, where the R^2 values are 0.95, 0.99, and 0.95, respectively. Low RMSE values indicate small root mean squared errors, meaning that the model predictions are close to the actual values. The RMSE for all datasets is 0.05. RRMSE expressed as a percentage also shows relatively small errors relative to the range of data, with values of 19.58% for the training set, 16.36% for the validation set, and 14.44% for the test set. Lower RRMSE values for the validation and test sets suggest good overall model performance and no signs of overfitting. Despite the small number of measurements, with only 33 data points, the network exhibits good metrics. Based on these parameters, it can be concluded that the neural network model performs very well. High PCC and R^2 values, along with low RMSE and RRMSE values, indicate accurate and stable predictions for the training, validation, and test sets. The relatively low RMSE indicates that the average deviation of the model predictions from the actual values is small. According to a previous study [48,49], the estimation accuracy can be divided into four categories based on the RRMSE criterion as follows: excellent (below 10%), good (10% to 20%), acceptable (20% to 30%), and unacceptable (above 30%). Thus, the RRMSE values indicate good precision within the model. The model appears to be well-fitted without signs of overfitting. These model evaluation metrics for the test and validation sets demonstrate the sufficient generalization capability of the ANN for new, unseen data, which is crucial for the practical application of the network.

Figure 8 presents a residuals plot against the predicted values, indicating that the largest portion of data yields estimation errors ranging from −0.15 to 0.1.

Figure 9 shows scatter plots which indicate that the trend line between the measured and predicted C_{wy} values follows the linear y = x line (45°) relatively closely, with slopes of 0.959, 1.0345, and 1.096, and low constants of 0.0097, 0.0003, and 0.0068 for the training,

test, and validation data, respectively. This means that predictions using the ANN are characterized by a fairly accurate prediction ability.

Table 6. Model evaluation metrics for the ANN.

PCC train [-]	0.98
PCC valid [-]	0.99
PCC test [-]	0.97
R^2 train [-]	0.95
R^2 valid [-]	0.99
R^2 test [-]	0.95
RMSE train [-]	0.05
RMSE valid [-]	0.05
RMSE test [-]	0.05
RRMSE train [%]	19.58
RRMSE valid [%]	16.36
RRMSE test [%]	14.44

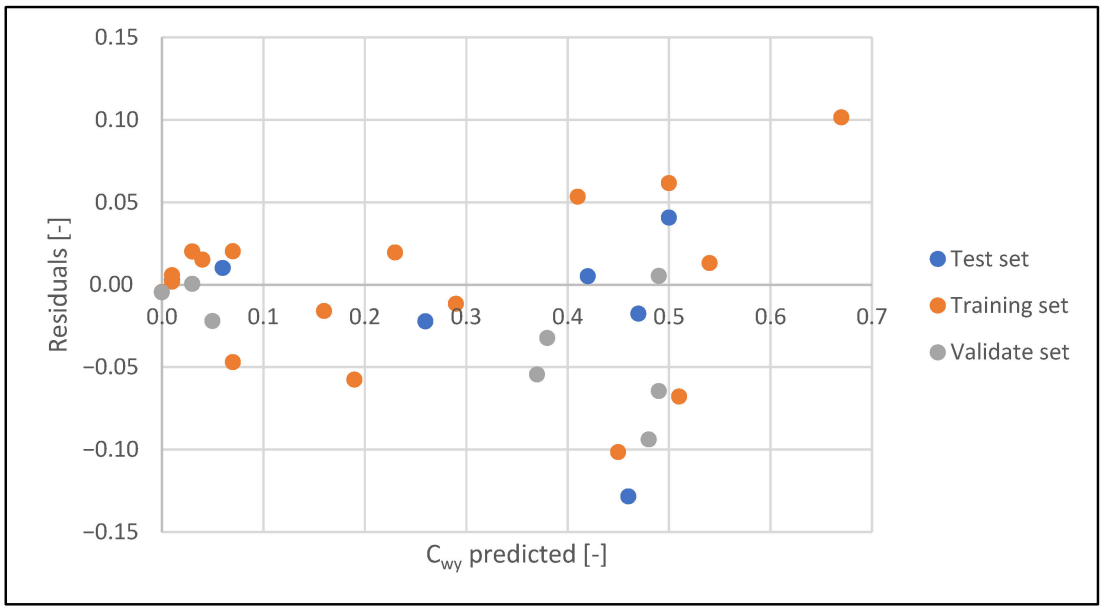

Figure 8. Residuals vs. predicted values.

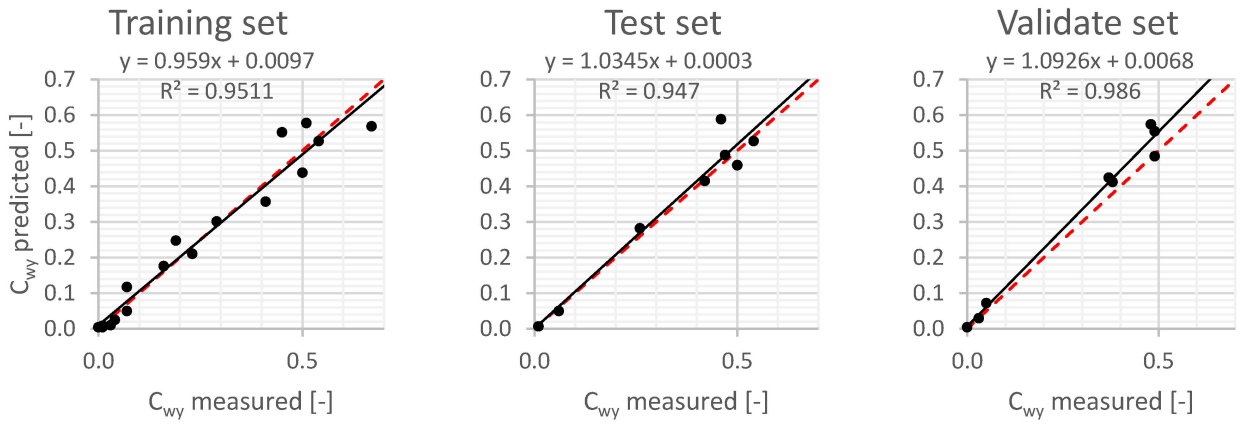

Figure 9. Scatter plots of predicted vs. measured C_{wy} values.

Figure 10 compares predictions made by the ANN with results from a model test. These plots show that the predictions obtained with the ANN are consistent with the test results and exhibit corresponding trends.

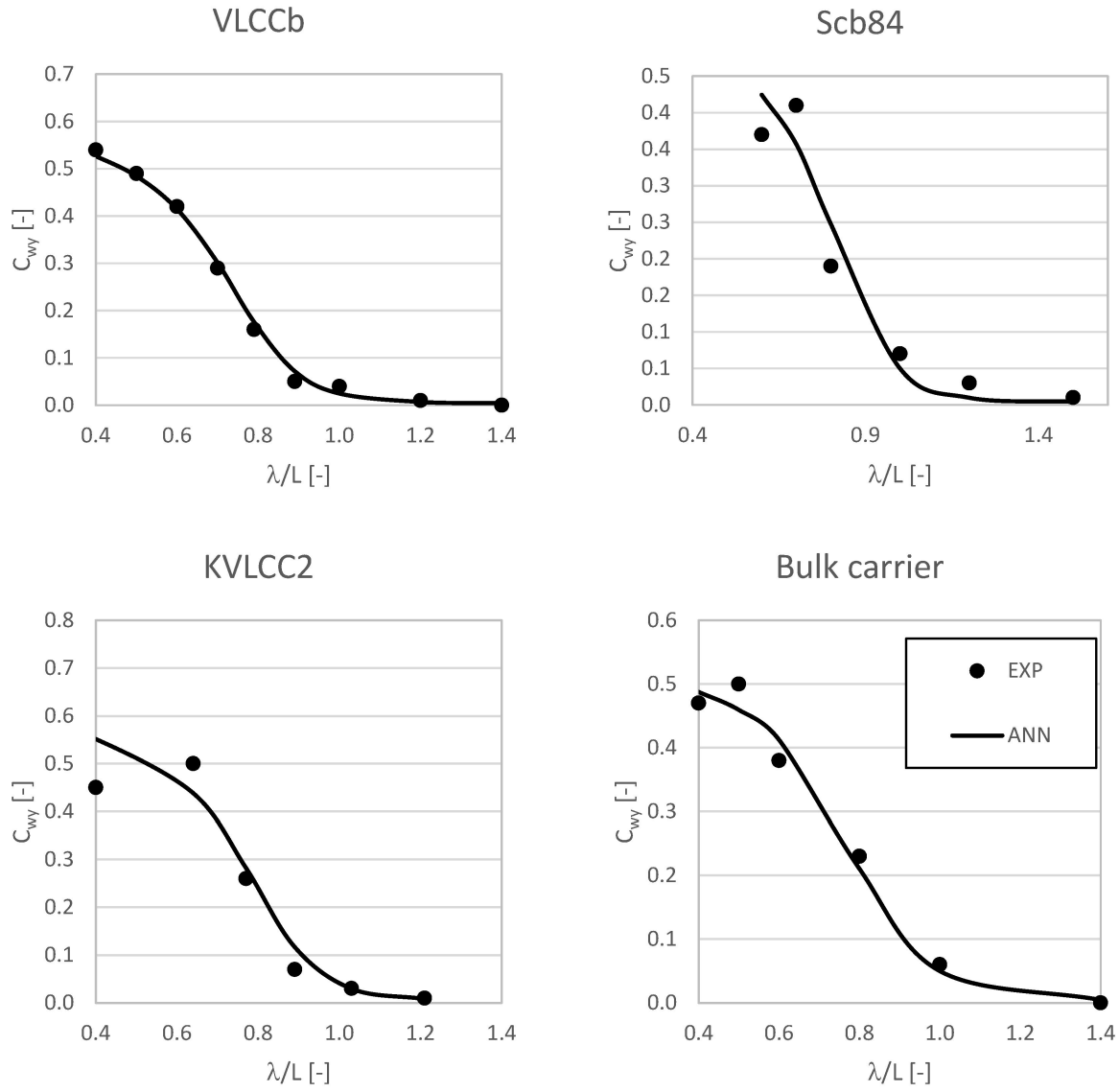

Figure 10. Comparison of ANN predictions with model test results.

Figure 11 presents predictions for fleets A, B, and C in relation to the data used for training the neural network. This Figure indicates that these predictions exhibit trends similar to those observed in the model test.

3.2. CO_2 Emissions during Nodule Loading in the CCZ

Using the developed ANN and Equations (8)–(11), wave-induced drift force values for bulk carriers A, B, and C were estimated by considering the significant wave height (Hs) and the average zero-up-crossing wave period (T_z) in the CCZ, as shown in Table 3. The results are presented in Tables A4–A6 in Appendix B. By applying Equation (7) and considering the wind speed distribution shown in Table 4, along with the characteristics of bulk carriers A, B, and C, the wind-induced drift forces were estimated. These are depicted in Figure 12.

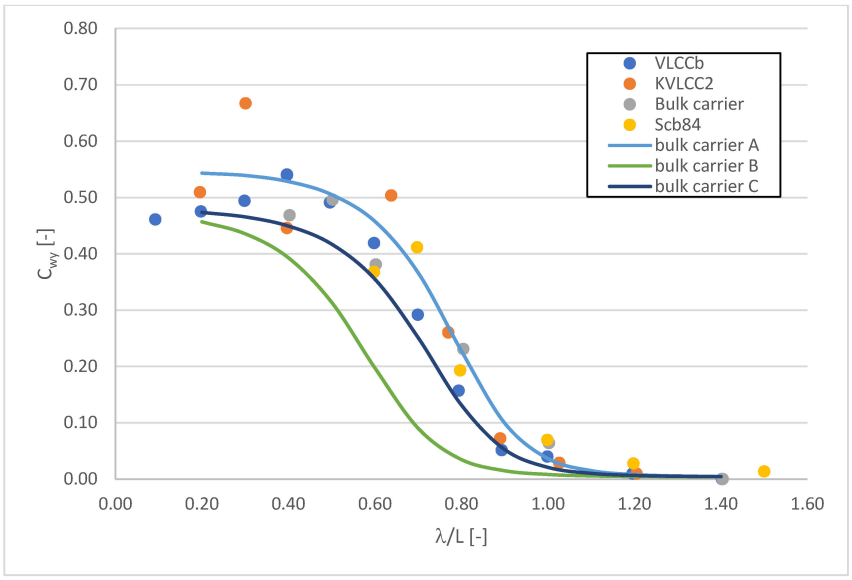

Figure 11. Comparison of ANN predictions for bulk carriers types A, B, and C with model test results.

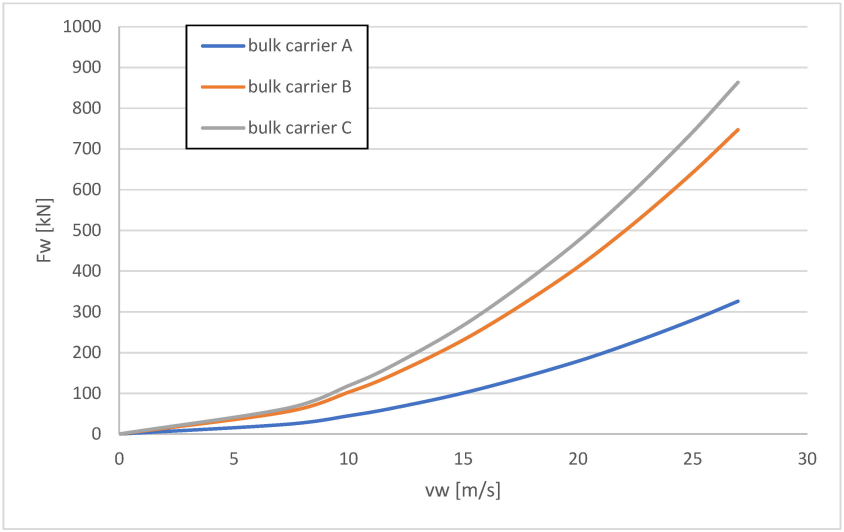

Figure 12. Drift force values from wind for bulk carriers A, B, and C which correspond to wind velocity (v_W).

When considering the most frequently occurring wave heights in the CCZ, which are 4 m according to Table 3, it is suggested that the largest drift forces, as shown in the figures and tables, are as follows:

- 775 kN, 1287 kN, and 1688 kN from waves,
- 106 kN, 244 kN, and 282 kN from wind,

for bulk carriers A, B, and C, respectively.

The thrust force (Tp) and the power (P) supplied to the propellers of the DP system were calculated using Equations (5) and (6). A power-to-thrust efficiency ratio (Cp) of 0.14 was assumed for the power calculations. Then, using Equations (3) and (17), the fuel consumption and the resulting CO_2 emissions of bulk carriers A, B, and C were calculated for 250 days a year during concrete loading operations in the CCZ.

Detailed values of fuel consumption resulting from the operation of the DP system to counteract the drift force caused by waves and wind on bulk carriers A, B, and C over 250 days a year during concrete loading in the CCZ can be found in Tables A7–A10 of Appendix B. The values of fuel consumption, which depend solely on Hs, are presented

collectively in Figure 13. This Figure illustrates that fuel consumption increases with wave height up to 3 m, reaching a maximum of 600 t, 1250 t, and 2100 t for bulk carriers A, B, and C, respectively. Beyond this level, fuel consumption decreases despite the increase in drift forces. This reduction in fuel consumption occurs because the amount of time the vessel spends in these conditions decreases as the wave height increases, given the lower occurrence of such large waves.

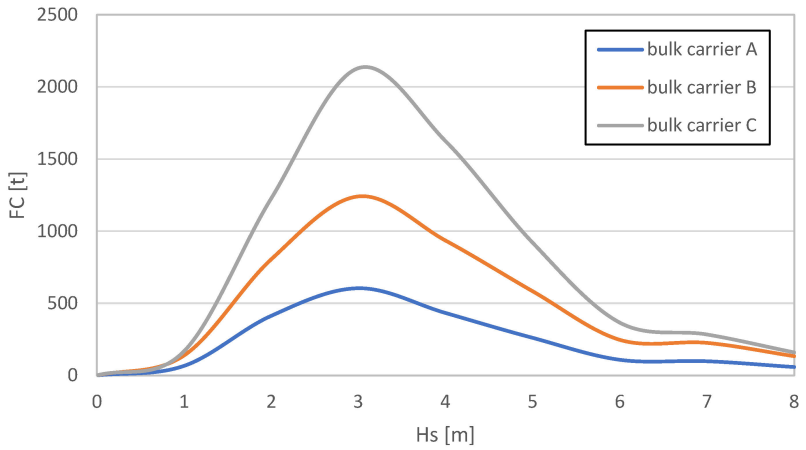

Figure 13. The values of fuel consumption (FC) [t] resulting from the operation of the DP system to counteract the drift force caused by wave and wind action on bulk carriers A, B, and C, corresponding to significant wave height (Hs).

Meanwhile, Figure 14 shows the cumulative CO_2 emissions from fuel combustion on ships due to wind and wave action as a function of wave height. For wave heights of up to 4 m, the cumulative CO_2 emissions are calculated to be 4900 t, 10,000 t, and 16,500 t for bulk carriers A, B, and C, respectively. These numbers demonstrate that significantly lower amounts of CO_2 will be emitted when using type A bulk carriers for the transshipment of extracted concrete. Utilizing type B and C bulk carriers for this mission will result in an increase in CO_2 emissions by 100% and 240%, respectively.

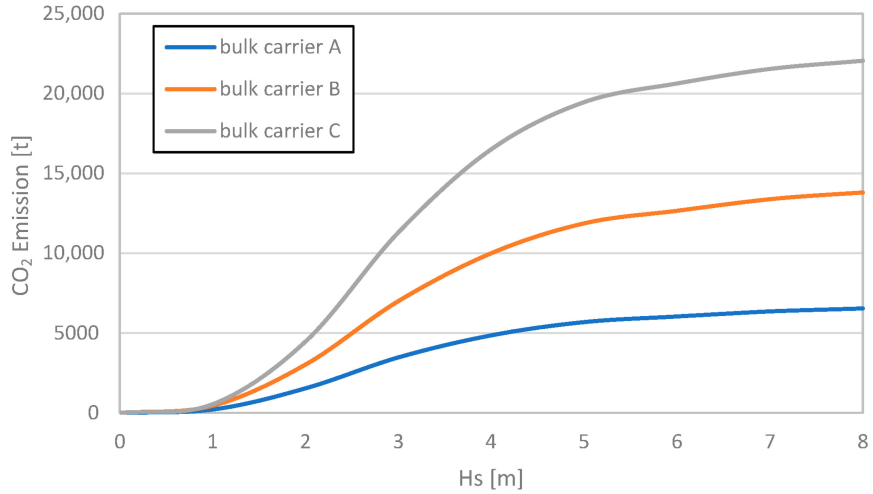

Figure 14. Cumulative CO_2 emissions due to combined wave and wind action in relation to significant wave height (Hs).

3.3. CO_2 Emissions during Transport

The number of shipments was calculated using Equation (21), based on the predetermined total mass of PMNs to be transported and the cargo capacities of bulk carriers A, B, and C. The results indicated that there were 264 shipments for bulk carrier A, 63 for B,

and 27 for C. Subsequently, utilizing the established routes shown in Figure 1, the distances that bulk carriers A, B, and C need to traverse to reach their designated destination ports were calculated based on Equations (20) and (21). The varying distances, according to the planned routes, are displayed in Table 7, which shows that type A bulk carriers are required to cover the longest distance, while type C has the shortest distance to traverse. These discrepancies increase with route length.

Table 7. Total distance to be covered by A, B, and C bulk carriers.

Route Number According to Figure 1	Route Length from the CC Zone to the Destination Port [NM]	Total Distance [NM]		
		A	B	C
1	2044	1,077,083	255,475	108,321
2	2400	1,264,800	300,000	127,200
3	6971	3,673,506	871,325	369,442
4	16,696	8,798,581	2,086,950	884,867
5	22,512	11,863,666	2,813,963	1,193,120
6	26,291	13,855,462	3,286,400	1,393,434

In accordance with a report by the International Maritime Organization [31], the threshold values for the energy efficiency design index (EEDI) were calculated using Equation (19), resulting in 9.48 for bulk carrier A, 4.78 for B, and 3.21 for C. This analysis shows that the largest bulk carriers have the lowest CO_2 emissions. Comparatively, type A and B bulk carriers emit nearly 200% and 50% more CO_2 than those of type C, respectively.

Based on these data, the total CO_2 emissions of bulk carriers A, B, and C, which transport the predetermined mass of PMNs to ports via designated routes, were calculated. The results, graphically presented in Figure 15, indicate that type C bulk carriers will emit the least amount of CO_2. Transporting the same amount of extracted PMNs to the farthest destination port using type C bulk carriers will result in CO_2 emissions of 998,768 tones, compared to 502,449 tones for type B and as much as 329,338 tones for type A. Therefore, transporting PMNs from the CC zone to the unloading port using type A and B bulk carriers will cause an increase in CO_2 emissions by 203% and 53%, respectively, when compared to using type C bulk carriers.

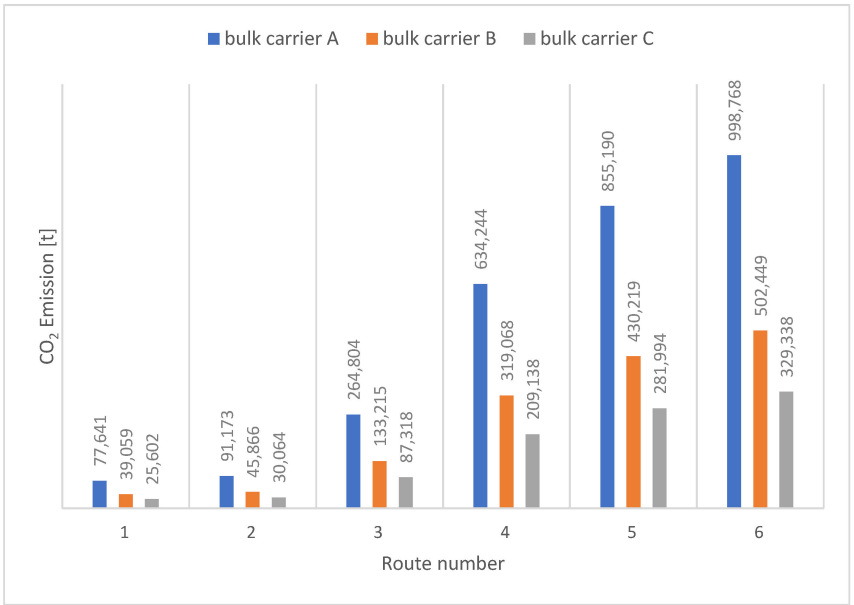

Figure 15. Total CO_2 emissions of A, B, and C bulk carriers during transportation.

3.4. Assessment of CO_2 Emissions from Bulk Carriers during Nodule Loading and Maritime Transport

Based on the CO_2 emissions of A, B, and C bulk carriers during the loading of PMNs in the CCZ and during transportation, the total CO_2 emissions for the entire mission were calculated. The calculations were conducted under the assumption that the loading in the CCZ is carried out with wave heights up to 3 m and wind speeds up to 12 m/s. The results are presented in Figure 16. On route number 1, which is the shortest, type A, B, and C bulk carriers emit 81,111, 46,058, and 36,902 tons of CO_2, respectively. On route number 6, which is the longest, A, B, and C bulk carriers emit 1,002,238, 509,449, and 340,638 tons of CO_2 together, respectively. Hence, it follows that, regardless of route length, the smallest bulk carriers emit the largest amount of CO_2, and the largest bulk carriers emit the least. Therefore, the amount of CO_2 emitted decreases with an increase in bulk carrier size. Moreover, the further the distance to the unloading port of PMNs, the greater the differences in CO_2 emissions in favor of large bulk carriers. On the shortest route, type A and B bulk carriers emit 120% and 25% more CO_2 than type C bulk carriers, respectively. On the longest route, type A and B bulk carriers emit 194% and 50% more CO_2 than type C bulk carriers, respectively.

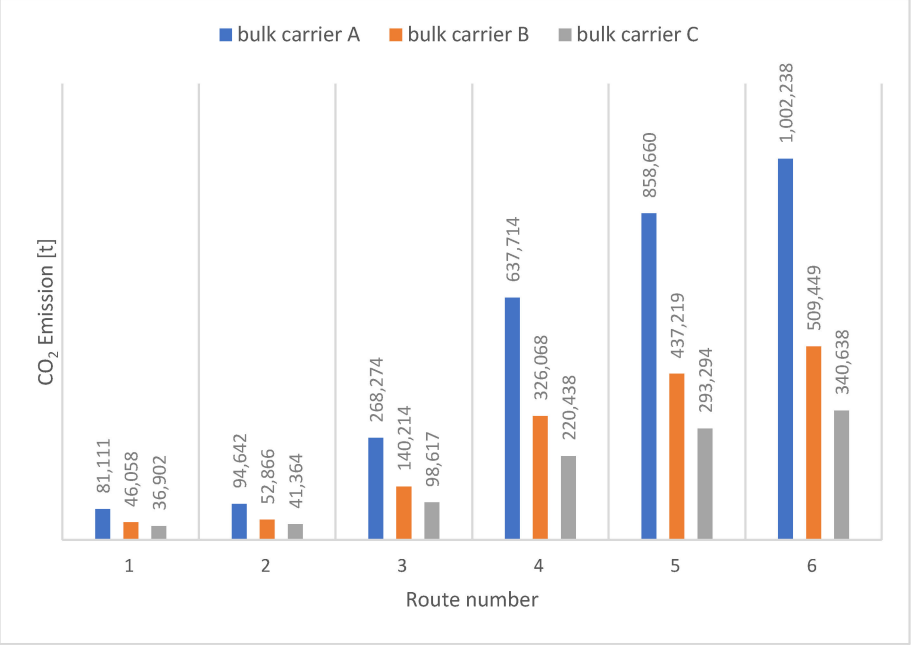

Figure 16. Total CO_2 emissions of A, B, and C bulk carriers during loading and transportation.

On the shortest route, the differences in CO_2 emissions between small and large bulk carriers are relatively minimal. Figure 17 shows the cumulative CO_2 emissions during the extraction and transportation of nodules to the nearest destination port, depending on the wave height (and corresponding wind speed) prevailing during the loading of nodules in the CC zone.

For the smallest bulk carriers, the impact of wind and waves on CO_2 emissions is minimal. This is due to the small size of these ships and the need for them to cover longer distances compared to larger ships, which significantly increases CO_2 emissions during the voyage. With wave heights up to 1 m and wind speeds up to 7 m/s, these ships emit 77,850 thousand tons of CO_2, and with wave heights of 5 m, they emit 83,300 thousand tons of CO_2, indicating an increase of only about 7%.

Environmental conditions have a greater impact on medium and large bulk carriers, as the influence of waves and wind on these ships is more significant, increasing CO_2 emissions, although the relative emissions during transport are lower. Loading nodules in wave heights up to 5 m and wind speeds up to 19 m/s results in annual CO_2 emissions

of 51,000 and 45,000 tons for bulk carriers type B and C, respectively. In contrast, loading nodules in wave heights up to 1 m and wind speeds up to 7 m/s results in annual CO_2 emissions of 39,500 and 26,100 tons for bulk carriers type B and C, respectively. When compared to emissions at 5 m wave heights, this represents an increase of approximately 29% for bulk carrier type B and as much as 72% for bulk carrier type C. For wave heights up to 2 m and wind speeds up to 10 m/s, the annual emissions are 42,000 and 30,000 tons of CO_2 for bulk carriers type B and C, respectively, which corresponds to an increase of approximately 21% for bulk carrier type B and 50% for bulk carrier type C when compared to emissions at 5 m wave heights.

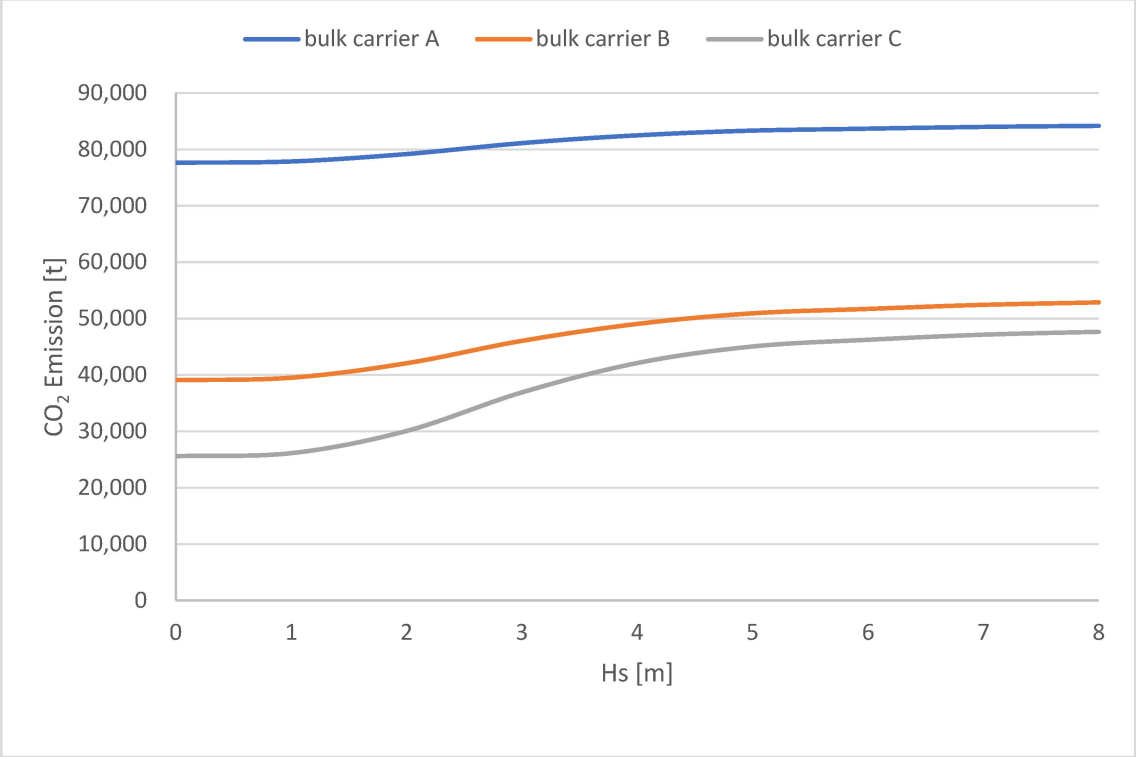

Figure 17. Cumulative CO_2 emissions of A, B, and C bulk carriers during loading and transportation on route no. 1, as influenced by environmental conditions represented by significant wave height (Hs).

Loading all types of ships in worse weather conditions, i.e., wave heights greater than 5 m and wind speeds above 19 m/s, does not significantly increase CO_2 emissions, as such conditions are relatively rare and the duration of the trips in these conditions is short.

Assuming that loading will be conducted in wave conditions up to 1–2 m due to technical issues related to ensuring safe loading, as indicated by [20,21], on the shortest route and on the largest bulk carriers, a significant impact of waves and wind on CO_2 emissions can be expected. However, on longer routes, this impact is not substantial.

4. Discussion

The analysis presented in the article indicates that the smallest type A bulk carriers, although characterized by a lower drift force, generate higher CO_2 emissions when compared to larger vessels. This is associated with their lower transport efficiency and the greater number of trips required to deliver nodules to the destination port, resulting in higher fuel consumption and, consequently, higher CO_2 emissions. In contrast, the largest type C bulk carriers, despite the greater drift force caused by marine environmental effects during loading, emit less CO_2 overall, thanks to their higher transport efficiency. These results suggest that selecting larger vessels for the loading and transporting of nodule cargo

can positively contribute to reducing the environmental impact of the mission by reducing carbon dioxide emissions.

These studies were conducted with the assumption that all types of ships can conduct loading operations efficiently, even in challenging weather conditions. However, research conducted by Kacprzak [20] has shown that the loading of PMNs on small bulk carriers can only be carried out under limited weather conditions. This means that the use of a fleet of small bulk carriers for the loading and transport of PMNs may lead to an extension of the time required to complete these operations due to the lower number of days in a year that are suitable for loading. These findings suggest that using large bulk carriers for these tasks may be a more efficient solution than using small ones.

Figures 15–17 show that the overall CO_2 emission related to the transport mission primarily depends on the emissions generated during sea transport. This clearly demonstrates that, although smaller ships may emit less CO_2 during the loading operations themselves, their lower transport efficiency, and the need to make a significantly larger number of voyages and thus cover a longer distance, means that when considering the entire venture, their environmental impact is negatively greater than that of large bulk carriers. Combined with the fact that small ships burn relatively more fuel per unit of transported cargo than large ones, this leads to the conclusion that the use of a fleet of large ships could be key from the point of view of ecological efficiency. This discovery may have significant implications for ecological policy in maritime transport. It shows that efforts to limit CO_2 emissions in maritime transport should not only include the search for new technologies and fuels, but also the optimization of fleet size and operation planning. Using large bulk carriers for the transportation of all types of cargo could significantly reduce global CO_2 emissions from maritime transport, presenting both a challenge and an opportunity for the industry.

Scaling the research findings to encompass general maritime transport clearly shows the substantial potential for reducing CO_2 emissions. This is particularly relevant given the feasibility of the annual transportation of up to 11 billion tons of cargo via sea, as reported in UNCTAD [68]. For example, Figure 18 depicts the hypothetical CO_2 emissions generated by ships carrying a volume of cargo along a typical route spanning an average of 5000 nautical miles in relation to the ship deadweight capacity. The illustration reveals that utilizing only a fleet of the smallest bulk carriers, each with a deadweight of 1000 tons, would culminate in an annual CO_2 emission totaling 1,960,843,563 tons. Conversely, only employing a fleet composed of the largest bulk carriers, each boasting a deadweight of 320,000 tons, would significantly reduce the annual CO_2 emission to merely 125,166,010 tons. Therefore, if we assume hypothetically that all the global cargo transported annually was only carried by the smallest bulk carriers, this will increase the emissions by 1,835,677,553 tons of CO_2 annually. This roughly equates to the annual burning of 1.142 billion passenger cars with an average consumption of 6 L of diesel per 100 km, assuming that they each travel 10,000 km annually. This example highlights the need for further research and analysis to better understand and utilize the potential for the efficient use of large bulk carriers in ecological maritime transport. The analysis presented in the article potentially represents a significant advancement in understanding the complexities of CO_2 emissions in maritime transport. It emphasizes that the ecological efficiency of this sector depends not only on the employed technologies, which primarily involve alternative fuels [69–71], but also on operational strategies and planning. Optimizing the size of ships could bring significant benefits to the environment, which should be considered in global efforts towards sustainable development and carbon footprint reduction. However, verifying this approach requires conducting more detailed research in this area, which may be explored in subsequent studies by the authors.

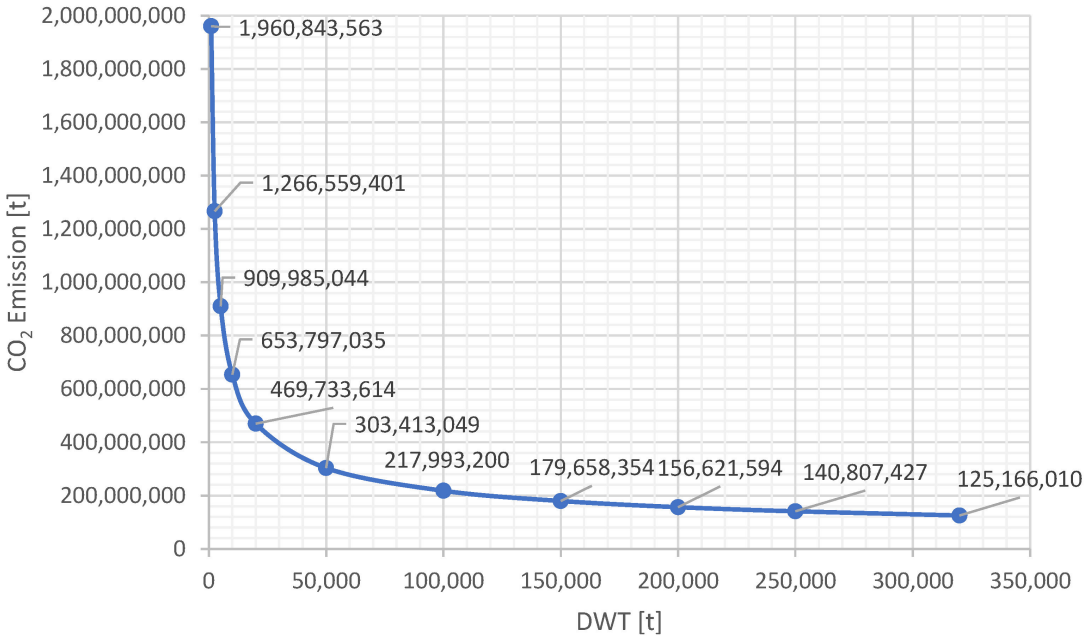

Figure 18. Comparative analysis of annual CO_2 emissions: smallest vs. largest bulk carriers on a 5000-nautical mile route transporting 11 billion tons of cargo.

5. Conclusions

The study confirmed the set objectives, providing significant insights into the impact of ship size on CO_2 emissions. It introduces new methods for assessing energy efficiency and the use of ANNs to estimate drifting force. The key innovations of the article include the following:

- the impact of bulk carrier size on CO_2 emissions, indicating the possibility of reducing the carbon footprint through the optimal selection of transport units,
- a new method to assess energy efficiency that takes environmental conditions into account, which can significantly contribute to the optimization of fuel consumption and the reduction of CO_2 emissions,
- the application of ANNs to estimate drifting force, offering new perspectives for ship design and operation, and highlighting the potential of artificial intelligence in the analysis of maritime operations.

The study demonstrated that large bulk carriers, despite the greater drift force acting on them, emit less CO_2 than smaller bulk carriers, both when considering the loading at sea of PMNs and their transport to the destination port. This indicates that preferring larger ships in global maritime trade can reduce environmental impacts due to their higher transport efficiency and lower CO_2 emissions.

The proposed method to estimate fuel consumption and CO_2 emissions, considering environmental conditions with the DP system, could lead to a new energy efficiency indicator. This indicator would aid in assessing and optimizing maritime operations from an environmental perspective, but also requires further research.

Using neural networks (ANNs) to estimate lateral drifting force in regular waves has proven effective, demonstrating its potential in maritime analysis. The developed ANN accurately predicts drifting force based on ship design parameters. However, practical use is limited by the narrow dimension ratio ranges of the training models. Expanding the training dataset with more diverse ship shapes could improve the method's universality, with further research required.

Author Contributions: All authors contributed equally to this editorial. All authors have read and agreed to the published version of the manuscript.

Funding: This research received no external funding.

Data Availability Statement: All data supporting the reported results are included in the attachments of this article. No new data were created during this study.

Conflicts of Interest: The authors declare no conflicts of interest.

Abbreviations

ANN	Artificial neural network
A_W	Lateral plane of the vessel above the plane of draught
B	Breadth of the ship
BFGS	Broyden–Fletcher–Goldfarb–Shanno algorithm
CB	Block coefficient
CCZ	Clarion-Clipperton Zone
CII	Carbon intensity indicator
CO_2	Carbon dioxide
D	Displacement
DP	Dynamic positioning
DWT	Deadweight tonnage
EEDI	Energy efficiency design index
EEOI	Energy efficiency operational indicator
Hs	Significant wave height
IMO	International Maritime Organization
L	Length between perpendiculars of the ship
MSE	Mean squared error
PCC	Pearson correlation coefficient
PMNs	Polymetallic nodules
RMSE	Root mean squared error
RRMSE	Relative root mean square error
SCG	Scaled conjugate gradient
SGD	Stochastic gradient descent
T	Draught of the ship
T_z	Average zero-up-crossing wave period
λ	Wavelength of a regular wave

Appendix A

Table A1. Normalization coefficients for the inputs and output of the ANN.

	Shift	Scale
L/B.	−30.6666666666666	5.55555555555554
B/T	−8.70967741935485	3.22580645161291
L/T	−12.5121951219512	0.81300813008130
CB	−27.0000000000001	33.3333333333334
l/L	−1.53846153846154	0.76923076923076
Output	0	1.49253731343284

Table A2. Neuron weights and biases in the hidden layer.

	Neuron in the Hidden Layer					
Input	**1**	**2**	**3**	**4**	**5**	**6**
L/B	0.301285	0.300698	0.193848	0.427797	0.160716	−0.070965
B/T	0.770441	0.370726	0.749137	0.094164	0.785890	−0.726824
L/T	0.794974	0.526635	1.035377	0.867195	1.019568	0.842477
CB	2.544873	1.573534	2.629856	2.722212	2.506663	−0.238512
l/L	3.111188	2.391626	3.641622	5.705001	4.086734	9.063809
bias	0.558491	0.400501	0.554879	−1.215970	0.480272	−4.862085

Table A3. Neuron weights and biases in the output layer.

	Output
Neuron 1	0.703693
Neuron 2	−0.501220
Neuron 3	1.014894
Neuron 4	−1.718017
Neuron 5	0.080677
Neuron 6	−6.121465
bias	1.356850

Appendix B

Table A4. Estimated drift force values from beam seas for bulk carrier type A using ANN.

Hs (m)	T_z (s)										
	<4	**4 to 5**	**5 to 6**	**6 to 7**	**7 to 8**	**8 to 9**	**9 to 10**	**10 to 11**	**11 to 12**	**12 to 13**	**>13**
7 to 8	2566	3303	2787	1960	1301	861	581	401	284	206	153
6 to 7	1965	2529	2134	1501	996	659	445	307	217	158	117
5 to 6	1443	1858	1568	1103	732	485	327	226	160	116	86
4 to 5	1002	1290	1089	766	508	336	227	157	111	80	60
3 to 4	642	826	697	490	325	215	145	100	71	52	38
2 to 3	361	464	392	276	183	121	82	56	40	29	21
1 to 2	160	206	174	123	81	54	36	25	18	13	10
0 to 1	40	52	44	31	20	13	9	6	4	3	2

Table A5. Estimated drift force values from beam seas for bulk carrier type B using ANN.

Hs (m)	T_z (s)										
	<4	**4 to 5**	**5 to 6**	**6 to 7**	**7 to 8**	**8 to 9**	**9 to 10**	**10 to 11**	**11 to 12**	**12 to 13**	**>13**
7 to 8	1232	3291	4043	3565	2717	1959	1393	996	722	532	398
6 to 7	943	2519	3095	2729	2080	1500	1067	763	553	407	305
5 to 6	693	1851	2274	2005	1528	1102	784	560	406	299	224
4 to 5	481	1285	1579	1393	1061	765	544	389	282	208	156
3 to 4	308	823	1011	891	679	490	348	249	181	133	100
2 to 3	173	463	568	501	382	275	196	140	102	75	56
1 to 2	77	206	253	223	170	122	87	62	45	33	25
0 to 1	19	51	63	56	42	31	22	16	11	8	6

Table A6. Estimated drift force values from beam seas for bulk carrier type C using ANN.

Hs (m)	T_z (s)										
	<4	**4 to 5**	**5 to 6**	**6 to 7**	**7 to 8**	**8 to 9**	**9 to 10**	**10 to 11**	**11 to 12**	**12 to 13**	**>13**
7 to 8	888	3352	5256	5689	5055	4040	3072	2293	1709	1283	974
6 to 7	680	2566	4024	4355	3871	3093	2352	1756	1309	982	746
5 to 6	499	1885	2957	3200	2844	2273	1728	1290	961	722	548
4 to 5	347	1309	2053	2222	1975	1578	1200	896	668	501	380
3 to 4	222	838	1314	1422	1264	1010	768	573	427	321	243
2 to 3	125	471	739	800	711	568	432	322	240	180	137
1 to 2	55	209	329	356	316	253	192	143	107	80	61
0 to 1	14	52	82	89	79	63	48	36	27	20	15

Table A7. Values of fuel consumption FC [t] resulting from the operation of the DP system to counteract the drift force caused by wave action on bulk carrier A.

Hs (m)	T_z (s)										
	<4	**4 to 5**	**5 to 6**	**6 to 7**	**7 to 8**	**8 to 9**	**9 to 10**	**10 to 11**	**11 to 12**	**12 to 13**	**>13**
7 to 8	0	0	0	0	0	1	0	0	0	0	0
6 to 7	0	0	0	0	2	3	3	2	1	0	0
5 to 6	0	0	0	3	9	11	9	4	2	1	0
4 to 5	0	0	3	16	35	37	23	10	4	1	0
3 to 4	0	1	14	63	103	84	42	15	4	1	0
2 to 3	0	3	48	147	165	96	36	10	2	0	0
1 to 2	0	10	71	116	76	28	7	1	0	0	0
0 to 1	0	3	7	5	1	0	0	0	0	0	0

Table A8. Values of fuel consumption FC [t] resulting from the operation of the DP system to counteract the drift force caused by wave action on bulk carrier B.

Hs (m)	T_z (s)										
	<4	**4 to 5**	**5 to 6**	**6 to 7**	**7 to 8**	**8 to 9**	**9 to 10**	**10 to 11**	**11 to 12**	**12 to 13**	**>13**
7 to 8	0	0	0	0	0	2	1	1	1	0	0
6 to 7	0	0	0	0	4	6	6	4	2	1	0
5 to 6	0	0	0	5	18	26	21	11	5	2	0
4 to 5	0	0	4	30	74	85	56	26	9	2	1
3 to 4	0	1	20	115	215	191	101	38	11	3	1
2 to 3	0	3	70	268	345	219	86	25	6	1	0
1 to 2	0	10	103	210	159	63	17	3	1	0	0
0 to 1	0	3	10	9	3	1	0	0	0	0	0

Table A9. Values of fuel consumption FC [t] resulting from the operation of the DP system to counteract the drift force caused by wave action on bulk carrier C.

Hs (m)	T_z (s)										
	<4	**4 to 5**	**5 to 6**	**6 to 7**	**7 to 8**	**8 to 9**	**9 to 10**	**10 to 11**	**11 to 12**	**12 to 13**	**>13**
7 to 8	0	0	0	0	0	3	3	2	1	1	0
6 to 7	0	0	0	0	7	13	14	9	4	2	1
5 to 6	0	0	0	8	34	53	46	25	11	4	1
4 to 5	0	0	5	48	137	175	123	59	21	6	2
3 to 4	0	1	26	183	401	394	223	86	26	6	1
2 to 3	0	3	91	427	642	452	190	56	13	3	0
1 to 2	0	10	133	335	296	131	37	8	1	0	0
0 to 1	0	3	13	14	6	1	0	0	0	0	0

Table A10. Values of fuel consumption (FC) [t] resulting from the operation of the DP system to counteract the drift force caused by wind on bulk carriers A, B, and C.

Hs (m)	v_W (m/s)	FC (t)		
		Bulk Carrier A	**Bulk Carrier B**	**Bulk Carrier C**
7 to 8	0	56	128	148
6 to 7	0	88	202	234
5 to 6	0	69	159	184
4 to 5	0	130	297	344
3 to 4	0	105	241	278
2 to 3	0	95	218	252
1 to 2	0	104	239	276
0 to 1	0	49	112	130

References

1. UNCTAD. Review of Maritime Transport (UNCTAD/RMT/2021). United Nations Conference on Trade and Development. 2021. Available online: https://unctad.org/publication/review-maritime-transport-2021 (accessed on 1 February 2024).
2. Fu, X.; Lang, J.; Wang, X.; Li, Y.; Lang, J.; Zhou, Y.; Guo, X. The impacts of ship emissions on ozone in eastern China. *Sci. Total Environ.* **2023**, *903*, 166252. [CrossRef] [PubMed]
3. Nunes, R.A.O.; Alvim-Ferraz, M.C.M.; Martins, F.G.; Sousa, S.I.V. Environmental and social valuation of shipping emissions on four ports of Portugal. *J. Environ. Manag.* **2019**, *235*, 62–69. [CrossRef] [PubMed]
4. Moreno-Gutiérrez, J.; Pájaro-Velázquez, E.; Amado-Sánchez, Y.; Rodríguez-Moreno, R.; Calderay-Cayetano, F.; Durán-Grados, V. Comparative analysis between different methods for calculating on-board ship's emissions and energy consumption based on operational data. *Sci. Total Environ.* **2019**, *650*, 575–584. [CrossRef] [PubMed]
5. Hoang, A.T.; Foley, A.M.; Nižetić, S.; Huang, Z.; Ong, H.C.; Ölçer, A.I.; Pham, V.V.; Nguyen, X.P. Energy-related approach for reduction of CO_2 emissions: A critical strategy on the port-to-ship pathway. *J. Clean. Prod.* **2022**, *355*, 131772. [CrossRef]
6. Fan, A.; Li, Y.; Liu, H.; Yang, L.; Tian, Z.; Li, Y.; Vladimir, N. Development trend and hotspot analysis of ship energy management. *J. Clean. Prod.* **2023**, *389*, 135899. [CrossRef]
7. Barone, G.; Buonomano, A.; Del Papa, G.; Maka, R.; Palombo, A. How to achieve energy efficiency and sustainability of large ships: A new tool to optimize the operation of on-board diesel generators. *Energy* **2023**, *282*, 128288. [CrossRef]
8. Nyanya, M.N.; Vu, H.B.; Schönborn, A.; Ölçer, A.I. Wind and solar assisted ship propulsion optimisation and its application to a bulk carrier. *Sustain. Energy Technol. Assess.* **2021**, *47*, 101397. [CrossRef]
9. Ytreberg, E.; Astrom, S.; Fridell, E. Valuating environmental impacts from ship emissions—The marine perspective. *J. Environ. Manag.* **2021**, *2021*, 111958. [CrossRef] [PubMed]
10. Amudha, K.; Bhattacharya, S.; Sharma, R.; Gopkumar, K.; Kumar, D.; Ramadass, G. Influence of flow area zone and vertical lift motion of polymetallic nodules in hydraulic collecting. *Ocean. Eng.* **2024**, *294*, 116745. [CrossRef]
11. Sha, F.; Xi, M.; Chen, X.; Liu, X.; Niu, H.; Zuo, Y. A recent review on multi-physics coupling between deep-sea mining equipment and marine sediment. *Ocean. Eng.* **2023**, *276*, 114229. [CrossRef]
12. Cunningham, A. Assessing the feasibility of deep-seabed mining of polymetallic nodules in the Area of seabed and ocean floor beyond the limits of national jurisdiction, as a method of alleviating supply-side issues for cobalt to US markets. *Miner. Econ.* **2024**, *37*, 207–226. [CrossRef]
13. Gollner, S.; Haeckel, M.; Janssen, F.; Lefaible, N.; Molari, M.; Papadopoulou, S.; Reichart, G.J.; Trabucho Alexandre, J.; Vink, A.; Vanreusel, A. Restoration experiments in polymetallic nodule areas. *Integr. Environ. Assess. Manag.* **2022**, *18*, 682–696. [CrossRef] [PubMed]
14. Bonifácio, P.; Kaiser, S.; Washburn, T.W.; Smith, C.R.; Vink, A.; Arbizu, P.M. Biodiversity of the Clarion-Clipperton Fracture Zone: A worm perspective. *Mar. Biodivers.* **2024**, *54*, 5. [CrossRef]
15. Uhlenkott, K.; Meyn, K.; Vink, A.; Martínez Arbizu, P. A review of megafauna diversity and abundance in an exploration area for polymetallic nodules in the eastern part of the Clarion Clipperton Fracture Zone (North East Pacific), and implications for potential future deep-sea mining in this area. *Mar. Biodivers.* **2023**, *53*, 22. [CrossRef]
16. Stratmann, T. Role of polymetallic-nodule dependent fauna on carbon cycling in the eastern Clarion-Clipperton Fracture Zone (Pacific). *Front. Mar. Sci.* **2023**, *10*, 1151442. [CrossRef]
17. Li, B.; Jia, Y.; Fan, Z.; Li, K.; Shi, X. Impact of the Mining Process on the Near-Seabed Environment of a Polymetallic Nodule Area: A Field Simulation Experiment in a Western Pacific Area. *Sensors* **2023**, *23*, 8110. [CrossRef] [PubMed]
18. Katona, S.; Paulikas, D.; Stone, G.S. Ethical opportunities in deep-sea collection of polymetallic nodules from the Clarion-Clipperton Zone. *Integr. Environ. Assess. Manag.* **2022**, *18*, 634–654. [CrossRef]
19. Shobayo, P.; van Hassel, E.; Vanelslander, T. Logistical Assessment of Deep-Sea Polymetallic Nodules Transport from an Offshore to an Onshore Location Using a Multiobjective Optimization Approach. *Sustainability* **2023**, *15*, 11317. [CrossRef]
20. Kacprzak, P. Assessment of cargo handling operation efficiency in the CCZ for standard bulk carriers in the view of significant amplitudes of roll as a limiting criterion. *Sci. J. Marit. Univ. Szczec.* **2023**, *74*, 55–64. [CrossRef]
21. Kacprzak, P. An analysis of shear forces, bending moments and roll motion during a nodule loading simulation for a ship at sea in the Clarion—Clipperton Zone. *Sci. J. Marit. Univ. Szczec.* **2021**, *65*, 9–20. [CrossRef]
22. Marques, C.H.; Belchiora, C.R.P.; Capracea, J.-D. Optimising the engine-propeller matching for a liquefied natural gas carrier T under rough weather. *Appl. Energy* **2018**, *232*, 187–196. [CrossRef]
23. Jurdziński, M. Processes of a freely drifting vessel. *TransNav* **2020**, *14*, 687–693. [CrossRef]
24. Bialystocki, N.; Konovessis, D. On the estimation of ship's fuel consumption and speed curve: A statistical approach. *J. Ocean. Eng. Sci.* **2016**, *1*, 157–166. [CrossRef]
25. Bal Beşikçi, E.; Arslan, O.; Turan, O.; Ölçer, A. An ANN based decision support system for energy efficient ship operations. *Comput. Oper. Res.* **2016**, *66*, 393–401. [CrossRef]
26. Petersen, J.P.; Jacobsen, D.J.; Winther, O. Statistical modelling for ship propulsion efficiency. *J. Mar. Sci. Technol.* **2011**, *17*, 30–39. [CrossRef]
27. Cepowski, T.; Drozd, A. Measurement-based relationships between container ship operating parameters and fuel consumption. *Appl. Energy* **2023**, *347*, 121315. [CrossRef]

28. Panagakos, G.; de Pessôa, T.S.; Dessypris, N.; Barfod, M.B.; Psaraftis, H.N. Monitoring the carbon footprint of dry bulk shipping in the EU: An early assessment of the MRV regulation. *Sustainability* **2019**, *11*, 5133. [CrossRef]
29. Kanberoğlu, B.; Kökkülünk, G. Assessment of CO_2 emissions for a bulk carrier fleet. *J. Clean. Prod.* **2021**, *283*, 124590. [CrossRef]
30. IMO. *Resolution MEPC.1/Circ.684 Guidelines for Voluntary Use of The Ship Energy Efficiency Operational Indicator (EEOI)*; IMO: London, UK, 2009.
31. IMO. *Resolution Res MEPC.364(79) Guidelines on the Method of Calculation of the Attained Energy Efficiency Design Index (EEDI) for New Ships*; IMO: London, UK, 2022.
32. IMO. *Resolution MEPC.346(78) Guidelines for the Development of a Ship Energy Efficiency. Management Plan (SEEMP)*; IMO: London, UK, 2022.
33. IMO. *Resolution MEPC.336(76) Guidelines on Operational Carbon Intensity Indicators and the Calculation Methods (CII GUIDELINES, G1)*; IMO: London, UK, 2021.
34. Chen, X.; Lv, S.; Shang, W.; Wu, H.; Xian, J.; Song, C. Ship energy consumption analysis and carbon emission exploitation via spatial-temporal maritime data. *Appl. Energy* **2024**, *360*, 122886. [CrossRef]
35. Lee, S.-S. Analysis of the effects of EEDI and EEXI implementation on CO2 emissions reduction in ships. *Ocean. Eng.* **2024**, *295*, 116877. [CrossRef]
36. Van Laar, G. Sustainable Transport of Polymetallic Nodules [TU Delft]. 2021. Available online: https://repository.tudelft.nl/islandora/object/uuid:ac42edba-a4ca-49ec-bb99-1c1b0b203f20 (accessed on 3 February 2024).
37. Lipton, I.T.; Nimmo, M.J. NI 43-101 Technical Report TOML Clarion Clipperton Zone Project, Pacific Ocean (Issue July). 2016. Available online: https://int.nyt.com/data/documenttools/2021-03-metals-company-technical-report-on-toml-mining-zone-plan/2d5350243bade994/full.pdf (accessed on 8 February 2024).
38. Dudziak, J. *Teoria Okrętu (II)*; Fundacja Promocji Przemysłu Okrętowego i Gospodarki Morskiej: Gdańsk, Poland, 2008; ISBN 978-83-60584-09-5.
39. Kadomatsu, K.; Inoue, Y.; Takarada, N. On the Required Minimum Output of Main Propulsion Engine for Large Fat Ship with Considering Manoeuverability in Rough Seas. *J. Soc. Nav. Arch. Jpn.* **1990**, *1990*, 171–182. [CrossRef] [PubMed]
40. Sprenger, F.; Maron, A.; Delefortrie, G.; Van Zwijnsvoorde, T.; Cura-Hochbaum, A.; Lengwinat, A.; Papanikolaou, A. Experimental Studies on Seakeeping and Manoeuvrability in Adverse Conditions. *J. Ship Res.* **2017**, *61*, 131–152. [CrossRef]
41. Shigunov, V.; El Moctar, O.; Papanikolaou, A.; Pottho, R.; Liu, S. International benchmark study on numerical simulation methods for prediction of manoeuvrability of ships in waves. *Ocean Eng.* **2018**, *165*, 365–385. [CrossRef]
42. Yasukawa, H.; Hirata, N.; Matsumoto, A.; Kuroiwa, R.; Mizokami, S. Evaluations of wave-induced steady forces and turning motion of a full hull ship in waves. *J. Mar. Sci. Technol.* **2018**, *24*, 1–15. [CrossRef]
43. Ueno, M.; Nimura, T.; Miyazaki, H.; Nonaka, K. Steady Wave Forces and Moment Acting on Ships in Manoeuvring Motion in Short Waves. *J. Soc. Nav. Arch. Jpn.* **2000**, *2000*, 163–172. [CrossRef] [PubMed]
44. Ueno, M.; Nimura, T.; Miyazaki, H.; Nonaka, K.; Haraguchi, T. Model Experiment on Steady Wave Forces and Moment Acting on a Ship a Rest. *J. Kansai Soc. Nav. Archit.* **2001**, *235*, 69–77.
45. Bortnowska, M. The Determination of Power Output of the Tracking Control System of a Mining Ship Zeszyty Naukowe NR 10 Akademii Morskiej W Szczecinie. *Sci. J. Marit. Univ. Szczec.* **2006**, *10*, 97–106.
46. ITTC. ITTC—Recommended Procedures and Guidelines-Seakeeping Experiments. In Proceedings of the 27th ITTC Seakeeping Committee, Copenhagen, Denmark, 31 August–5 September 2014; pp. 1–22.
47. Maruo, H. The drift of a body floating on waves. *J. Ship Res.* **1960**, *4*, 1–10.
48. Newman, J.N. The drift force and moment on ships in waves. *J. Ship Res.* **1967**, *11*, 51–60. [CrossRef]
49. Salvesen, N. Second-Order Steady State Forces and Moments on Surface Ships in Oblique Regular Waves. In International Symposium on Dynamics of Marine Vehicles and Structures in Waves. *Mech. Eng.* **1974**, *22*, 225–241.
50. Gerritsma, J.; Beukelman, W. Analysis of the resistance increase in waves of a fast cargo ship 12. *Int. Shipbuild. Prog.* **1972**, *19*, 285–293. [CrossRef]
51. Kashiwagi, M. Added Resistance, Wave-Induced Steady Sway Force and Yaw Moment on an Advancing Ship. *Ship Technol. Res. (Schistech.)* **1992**, *39*, 3–16.
52. Boese, P. Eine einfache Methode zur Berechnung der Widerstandserhöhung eines Schiffes im Seegang. *Ship Technol. Res.* **1970**, *258*, 17.
53. Faltinsen, O.M.; Minsaas, K.J.; Liapis, N.; Skjordal, S.O. Prediction of Resistance and Propulsion of a Ship in a Seaway. In Proceedings of the 13th Symposium on Naval Hydrodynamics, Tokyo, Japan, 6–10 October 1980; pp. 505–529.
54. Papanikolaou, A.; Nowacki, Z. Second-Order Theory of Oscillating Cylinders in a Regular Steep Wave. In Proceedings of the l3th ONR Symp., Tokyo, Japan, 6–10 October 1980; pp. 303–333.
55. Liu, S.; Papanikolaou, A. Prediction of the Side Drift Force of Full Ships Advancing in Waves at Low Speeds. *J. Mar. Sci. Eng.* **2020**, *8*, 377. [CrossRef]
56. Cepowski, T. The prediction of ship added resistance at the preliminary design stage by the use of an artificial neural network. *Ocean. Eng.* **2020**, *195*, 106657. [CrossRef]
57. Cepowski, T. The use of a set of artificial neural networks to predict added resistance in head waves at the parametric ship design stage. *Ocean. Eng.* **2023**, *281*, 114744. [CrossRef]

58. Ahn, Y.; Kim, Y. Data mining in sloshing experiment database and application of neural network for extreme load prediction. *Mar. Struct.* **2021**, *80*, 103074. [CrossRef]
59. Dyer, A.S.; Zaengle, D.; Nelson, J.R.; Duran, R.; Wenzlick, M.; Wingo, P.C.; Bauer, J.R.; Rose, K.; Romeo, L. Applied machine learning model comparison: Predicting offshore platform integrity with gradient boosting algorithms and neural networks. *Mar. Struct.* **2022**, *83*, 103152. [CrossRef]
60. Citakoglu, H.; Coşkun, Ö. Comparison of hybrid machine learning methods for the prediction of short-term meteorological droughts of Sakarya Meteorological Station in Turkey. *Environ. Sci. Pollut. Res.* **2022**, *29*, 75487–75511. [CrossRef]
61. Demir, V.; Citakoglu, H. Forecasting of solar radiation using different machine learning approaches. *Neural Comput. Applic.* **2023**, *35*, 887–906. [CrossRef]
62. Premalatha, M.; Naveen, C. Analysis of different combi- nations of meteorological parameters in predicting the horizontal global solar radiation with ann approach: A case study. *Renew. Sustain. Energy Rev.* **2018**, *91*, 248–258. [CrossRef]
63. Uncuoglu, E.; Citakoglu, H.; Latifoglu, L.; Bayram, S.; Laman, M.; Ilkentapar, M.; Oner, A.A. Comparison of neural network, Gaussian regression, support vector machine, long short-term memory, multi-gene genetic programming, and M5 Trees methods for solving civil enginee *Energies* ring problems. *Appl. Soft Comput.* **2022**, *129*, 109623. [CrossRef]
64. Broyden, C.G. The convergence of a class of double-rank minimization algorithms 1. General considerations. *IMA J. Appl. Math.* **1970**, *6*, 76–90. [CrossRef]
65. Fletcher, R. A new approach to variable metric algorithms. *Comput. J.* **1970**, *13*, 317–322. [CrossRef]
66. Goldfarb, D. A family of variable-metric methods derived by variational means. *Math. Comput.* **1970**, *24*, 23–26. [CrossRef]
67. Shanno, D.F. Conditioning of quasi-newton methods for function minimization. *Math. Comput.* **1970**, *24*, 647–656. [CrossRef]
68. UNCTAD. Review of Maritime Transport (UNCTAD/RMT/2023). United Nations Conference on Trade and Development. 2023. Available online: https://unctad.org/publication/review-maritime-transport-2023 (accessed on 2 March 2024).
69. Obydenkova, S.V.; Defauw, L.V.E.; Kouris, P.D.; Smeulders, D.M.J.; Boot, M.D.; van der Meer, Y. Environmental and Economic Assessment of a Novel Solvolysis-Based Biorefinery Producing Lignin-Derived Marine Biofuel and Cellulosic Ethanol. *Energies* **2022**, *15*, 5007. [CrossRef]
70. Bortuzzo, V.; Bertagna, S.; Bucci, V. Mitigation of CO_2 Emissions from Commercial Ships: Evaluation of the Technology Readiness Level of Carbon Capture Systems. *Energies* **2023**, *16*, 3646. [CrossRef]
71. Richter, S.; Braun-Unkhoff, M.; Hasselwander, S.; Haas, S. Evaluation of the Applicability of Synthetic Fuels and Their Life Cycle Analyses. *Energies* **2024**, *17*, 981. [CrossRef]